Study of a Nonlinear Parabolic Problem by Compactness Method

MEFLAH Mabrouk

Université Kasdi Merbah de Ouargla, Algeria

Faculté des Mathématiques et des Sciences de la Matière

Laboratoire des Mathématiques Appliquées,Ouargla 30000.

E-mail: meflah.mabrouk@univ-ouargla

Abstract

In this work we will study a boundary value problem governed by a nonlinear heat equation by compactness method. We look for the existence and uniqueness of a function $u = u(x,t)$, $x \in \Omega$, $t \in (0,T)$, solution of the problem (P).

Keywords: Compactness, Nonlinear, Parabolic, Priori Estimates, Uniqueness.

1 Notations and position of the problem

Let Ω an open bounded domain of $\mathbb{R}^n$, with regular boundary Γ. We denot by Q the cylinder $\mathbb{R}^n_x \times \mathbb{R}_t : Q = \Omega \times]0,T[$, with boundary Σ, u_0 and f are functions, $\rho > 0$ .We look for the existence and uniqueness of a function $u = u(x,t)$, $x \in \Omega$, $t \in]0,T[$, solution of the problem (P).

$$(P) \begin{cases} \frac{\partial u}{\partial t} - \Delta u + |u|^\rho u = f & \text{in } Q \quad (1.1.1) \\ u = 0 & \text{on } \Sigma \ (1.1.2) \\ u(x,0) = u_0(x) & x \in \Omega \quad (1.1.3) \end{cases} \quad (1.1)$$

2 Existence and uniqueness of the solution

The main results are given by the fallowing theorem of existence and theorem of uniqueness

2.1 Existence of the solution

Theorem 1 *Assume that Ω is bounded open of $\mathbb{R}^n$ are given f, u_0 with .*

$$f \in L^2(Q), \quad (1.2)$$

$$u_0 \in H_0^1(\Omega) \cap L^p(\Omega), \ p = \rho + 2., \quad (1.3)$$

Then there exists a function u satisfying:

$$u \in L^\infty \left(0, T; H_0^1 \left(\Omega \right) \cap L^p \left(\Omega \right) \right), \tag{1.4}$$

$$\frac{\partial u}{\partial t}(x, 0) \in L^\infty \left(0, T; L^2 \left(\Omega \right) \right), \tag{1.5}$$

$$\frac{\partial u}{\partial t} - \Delta u + |u|^\rho u = f \ in \ Q \tag{1.6}$$

$$u(0) = u_0(x), \ x \in \Omega \tag{1.7}$$

Proof. ■

2.1.1 First step: looking for approached solutions

We introduce a sequence functions $w_1, ..., w_m, ..$ having the following properties:

$$\begin{cases} w_i \in H_0^1 \left(\Omega \right) \cap L^p \left(\Omega \right) \quad \forall i; \\ \forall m, \ w_1, ..., \ w_m \ \text{are linearly independent} \\ \text{combinations of linear finite } w_i \ \text{are dense in} \\ \quad H_0^1 \left(\Omega \right) \cap L^p \left(\Omega \right). \end{cases} \tag{1.8}$$

We look for $u_m = u_m \left(t \right)$ (approximate solution) of the problem as:

$$u_m \left(t \right) = \sum_{i=1}^{i=m} g_{im}(t) w_i. \tag{1.9}$$

We determine the functions g_{im} with the conditions

$$\left(u_m' \left(t \right), w_j \right) + a \left(u_m \left(t \right), w_j \right) + \left(|u_m \left(t \right)|^\rho u_m \left(t \right), w_j \right) = \left(f \left(t \right), w_j \right), \ 1 \leq j \leq m, \tag{1.10}$$

As a is a bilinear form defined as follows:

$$a \left(u, v \right) = \sum_{i=1}^{n} \int_\Omega \frac{\partial u}{\partial x_i} \frac{\partial v}{\partial x_i} dx \tag{1.11}$$

The system (1.10) of ordinary differential equations nonlinear be supplemented by initial conditions:

$$u_m \left(0 \right) = u_{0m}, \ u_{0m} = \sum_{i=1}^{m} \alpha_{im} w_i \underset{m \to \infty}{\to} u_0 \ in \ H_0^1 \left(\Omega \right) \cap L^p \left(\Omega \right), \tag{1.12}$$

Through the linear independence of $w_1, ..., w_m,$, we have $\det \left(w_i, w_j \right) \neq 0$, ie the system composed of $(1.10), (1.12)$ admits a solution defined on $[0, t_m]$. The a priori estimates which follow show that $t_m = T$.

2.1.2 Second step: a priori estimates.

We multiply equation (1.10) index j by $g'_{jm}(t)$ was:

$$(u'_m(t), u'_m(t)) + a(u_m(t), u'_m(t)) + (|u_m(t)|^\rho u_m(t), u'_m(t))$$

$$= (f(t), u'_m(t)) \tag{1.13}$$

But, $|u_m(t)|^\rho u_m(t) \in L^{p'}(\Omega)$ and $p = \rho + 2$, Then according to Cauchy Schwarz were:

$$\frac{1}{2}\frac{d}{dt}\left(|u'_m(t)|^2 + \|u_m(t)\|^2\right) + \frac{1}{p}\frac{d}{dt}\left(\int_\Omega |u_m(x,t)|^p dx\right) \leq |f(t)|\,|u'_m(t)|$$

$$\tag{1.14}$$

So we integrate between $0, t$, we deduce:

$$\frac{1}{2}\left(|u'_m(t)|^2 + \|u_m(t)\|^2\right) + \frac{1}{p}\|u_m(x,t)\|^p_{L^p(\Omega)} \leq \frac{1}{2}|u_{1m}|^2 + \frac{1}{2}\|u_{0m}\|^2$$

$$+\frac{1}{p}\|u_m(0)\|^p_{L^p(\Omega)} + \int_0^t |f(\sigma)|\,|u'_m(\sigma)|\,d\sigma \tag{1.15}$$

From $(17), (18)$ and inequality:

$$ab \leq \frac{1}{2}a^2 + \frac{1}{2}b^2.$$

We have

$$|f(\sigma)|\,|u'_m(\sigma)| \leq \frac{1}{2}|f(\sigma)|^2 + \frac{1}{2}|u'_m(\sigma)|^2.$$

Then

$$\frac{1}{2}\left(|u'_m(\sigma)|^2 + \|u_m(t)\|^2\right) + \frac{1}{p}\|u_m(x,t)\|^p_{L^p(\Omega)} \leq c + \frac{1}{2}\int_0^t |f(\sigma)|^2 d\sigma$$

$$+\frac{1}{2}\int_0^t |u'_m(\sigma)|^2 d\sigma. \tag{1.16}$$

But

$$f \in L^2(Q) \Rightarrow \int_0^t |f(\sigma)|^2 d\sigma \leq \text{constant}.$$

We deduce, therefore, in particular (1.16) that:

$$|u'_m(t)|^2 \leq c' + \int_0^t |u'_m(\sigma)|^2 \, d\sigma, \qquad (1.17)$$

And after the Gronwall inequality we have:

$$|u'_m(t)| \leq \text{constant}. \qquad (1.18)$$

Then

$$\|u_m(t)\| + \|u_m(x)\|_{L^p(\Omega)} \leq \text{constant}. \qquad (1.19)$$

By (1.18), (1.19) and when $m \to \infty$ we have: u_m in a bounded set of $L^\infty(0,T; H_0^1(\Omega) \cap L^p(\Omega))$ and u'_m in a bounded set of $L^\infty(0,T; L^2(\Omega))$.

2.1.3 Third step: passage to the limit

In the second step we were u_m borned in $L^\infty(0,T; H_0^1(\Omega) \cap L^p(\Omega))$, then it is bounded in $L^2(0,T; H_0^1(\Omega))$.Since $L^\infty(0,T; H_0^1(\Omega) \cap L^p(\Omega))$.{resp. $L^\infty(0,T; L^2(\Omega))$} is the dual of $L^1(0,T; H^{-1}(\Omega) + L^{p'}(\Omega))$ {resp. of $L^1(0,T; L^2(\Omega))$}, there exists a result u_m, u_μ sush that :

$$\forall g \in L^1\left(0,T; H^{-1}(\Omega) + L^{p'}(\Omega)\right) : .$$

$$\int_0^T (u_\mu(t), g(t)) \, dt \underset{\mu \to \infty}{\to} \int_0^T (u(t), g(t)) \, dt$$

Which implies:

$$u_\mu \to u \quad \text{weak in } L^\infty\left(0,T; H_0^1(\Omega) \cap L^p(\Omega)\right) \text{ and in } L^2\left(0,T; H_0^1(\Omega)\right). \qquad (1.20)$$

So :

$$\exists u'_\mu \to u' \text{in } D'\left(0,T; H_0^1(\Omega) \cap L^p(\Omega)\right) \Rightarrow u'_\mu \to u' \text{in } L^\infty\left(0,T; L^2(\Omega)\right)$$

$$\text{and in } L^2\left(0,T; L^2(\Omega)\right) \qquad (1.21)$$

Then in particular u_m bounded in $H^1(Q)$, but we know that the next injection is compact:

$$H^1(Q) \hookrightarrow L^2(Q) \qquad (1.22)$$

And according to the definition of compact injection, we can suppose the sequence u_μ extracted u_m satisfies (1.20) and (1.21), then u, u' exists and in $L^2(Q)$ then:

$$\begin{cases} u_\mu \to u \text{ in } L^2\left(0, T; H_0^1\left(\Omega\right) \cap L^p\left(\Omega\right)\right) \text{ strong (a.e)}, \\ \quad u'_\mu \to u' \text{in } L^2\left(0, T; L^2\left(\Omega\right)\right) \text{ weak (a.e)}. \end{cases} \quad (1.23)$$

Studying the convergence of $|u_m|^\rho u_m$:
$|u_m|^\rho u_m$ is bounded in $L^\infty\left(0, T; L^{p'}\left(\Omega\right)\right)$, then we set:

$$|u_\mu|^\rho u_\mu \to w \text{ in } L^\infty\left(0, T; L^{p'}\left(\Omega\right)\right), \quad (1.24)$$

Showing that:
$$w = |u|^\rho u. \quad (1.25)$$

For this we give the following lemma:

2.1.4 Lemma:

Let O be an open bounded $\mathbb{R}_x^n \times \mathbb{R}_t$, g_μ and g are functions of $L^q\left(O\right)$, $1 < q < \infty$, such that

$$\|g_\mu\|_{L^q(O)} \le c, \quad g_\mu \to g \text{ p.p. in } O \quad (1.26)$$

Then
$$g_\mu \to g \text{ in } L^q \text{ weak }. \quad (1.27)$$

When we ask: $O = Q$ and $g_\mu = |u_\mu|^\rho u_\mu$, from (1.23) :

$$u_\mu \to u \text{ in } L^2\left(Q\right) \text{ (a.e)} \quad (1.28)$$

Therefore :

$$g_\mu = |u_\mu|^\rho u_\mu \rightharpoonup |u|^\rho u = g \text{ (a.e) in } L^{p'}\left(\Omega\right) \quad (1.29)$$

Such that $p' = \frac{\rho+2}{\rho+1} = q$ (for $p = \rho + 2$), and after (1.24) :

$$|u_\mu|^\rho u_\mu \rightharpoonup w \text{ in } L^{p'}\left(\Omega\right). \quad (1.30)$$

Since the limit is unique, therefore:

$$g = |u|^\rho u = w.$$

We show that this solution satisfies the equation (1.10), so when we set $m = \mu$ and we fix j such that $\mu > j$; then:

$$\left(u'_\mu\left(t\right), w_j\right) + a\left(u_\mu, w_j\right) + \left(|u_\mu\left(t\right)|^\rho u_\mu\left(t\right), w_j\right) = \left(f\left(t\right), w_j\right). \quad (1.31)$$

From (1.24) and (1.25)

$$\left(u'_\mu, w_j\right) \rightharpoonup \left(u', w_j\right) \text{ in } L^\infty\left(0, T\right), \tag{1.32}$$

Where:

$$a\left(u_\mu, w_j\right) \rightharpoonup a\left(u, w_j\right) \text{ in } L^\infty\left(0, T\right). \tag{1.33}$$

And after (1.24) and (1.25)

$$\left(\left|u_\mu\right|^\rho u_\mu, w_j\right) \rightharpoonup \left(\left|u\right|^\rho u, w_j\right) \text{ in } L^\infty\left(0, T\right) \tag{1.34}$$

It follows therefore from (1.30) that:

$$\frac{d}{dt}\left(u, w_j\right) + a\left(u, w_j\right) + \left(\left|u\right|^\rho u, w_j\right) = \left(f, w_j\right). \tag{1.35}$$

According to the density of the basis $\{w_j\}$ in separable space $H_0^1\left(\Omega\right) \cap L^p\left(\Omega\right)$, we have

$$\frac{d}{dt}\left(u, v\right) + a\left(u, v\right) + \left(\left|u\right|^\rho u, v\right) = \left(f, v\right) \forall v \in H_0^1\left(\Omega\right) \cap L^p\left(\Omega\right) \tag{1.36}$$

Then the solution u satisfies (1.2), (1.3)

It remains to show that the solution u satisfies the initial conditions $(1.1.3): u\left(0\right) = u_0,$.

By (1.20) and (1.21) we have:

$$u_\mu \to u \text{ in } L^\infty\left(0, T; H_0^1\left(\Omega\right) \cap L^p\left(\Omega\right)\right), \tag{1.37}$$

So u_μ is continuous on $[0, T]$ then continous on 0 and then:

$$u_{0\mu} = u_\mu\left(0\right) \to u\left(0\right) = u_0 \text{ in } H_0^1\left(\Omega\right) \cap L^p\left(\Omega\right),$$

whence (1.7) .

3   Uniqueness of solution

Theorem 2

It is located in the assumptions of Theorem 1 with:

$$\rho \leq \frac{2}{n-2}$$

(any finite ρ if $n = 2$).Then the solution u obtained in Theorem of existence is unique.

Let u, v be two solutions, in the sense of Theorem 2, then $w = u - v$ satisfies:

$$\begin{cases} w' - \Delta w = |v|^\rho v - |u|^\rho u, \\ \quad w(0) = 0, \\ w \in L^\infty(0, T; H^1_0(\Omega) \cap L^p(\Omega)), \\ \quad w' \in L^\infty(0, T; L^2(\Omega)). \end{cases}$$

So (1.22) implies:

$$(w', v) + a(w, v) = (|v|^\rho v - |u|^\rho u, v) \quad \forall v \in H^1_0(\Omega).$$

To replace v by w' must $w' \in H^1_0(\Omega)$ for $v \in H^1_0(\Omega)$ but $w' \in L^2(\Omega)$ then we must introduce an auxiliary function:

$$\Psi :]0, T[\to \mathbb{R}, \ \forall s \in]0, T[$$

$$t \mapsto \Psi(t) = \begin{cases} -\int_t^s w(\sigma) d\sigma, \ t \le s; \\ \quad 0, \qquad t > s \end{cases}$$

$$\Psi'(t) = w(t); \quad w_1(t) = \int_0^t w(\sigma) d\sigma \text{ if } \forall t \le s.$$

Thus

$$\Psi(t) = -\int_t^s w(\sigma) d\sigma = w_1(t) - w_1(s) \Rightarrow \Psi(0) = -w_1(s)$$

Then (1.22) gives:

$$(w', \Psi(t)) + a(w, \Psi(t)) = (|v|^\rho v - |u|^\rho u, \Psi(t)) \Rightarrow$$

$$\frac{1}{2}|w(s)|^2 + \frac{1}{2}\|w_1(s)\|^2 = -\int_0^s (|v|^\rho v - |u|^\rho u, \Psi(t)) dt$$

We have

$$|-(|v|^\rho v - |u|^\rho u, \Psi(t))| \le c \int_\Omega \sup(|u|^\rho, |v|^\rho) |u - v| |\Psi(t)| dx =$$

$$c \int_\Omega \sup(|u|^\rho, |v|^\rho) |w(t)| |\Psi(t)| dx$$

According to Holder's inequality we have:

$$c \int_\Omega \sup\left(|u|^\rho, |v|^\rho\right) |w(t)| \, |\Psi(t)| \, dx = c \int_\Omega \sup\left(|u|^\rho, |v|^\rho\right) |w(t)|.$$

$$|w_1(t) - w_1(s)| \, dx \leq c \left[\left\| |u|^\rho \right\|_{L^n(\Omega)} + \left\| |v|^\rho \right\|_{L^n(\Omega)} \right]$$

As

$$\frac{1}{n} + \frac{1}{q} + \frac{1}{2} = 1,$$

Then

$$\frac{1}{q} = \frac{n-2}{2n} \Rightarrow q = \frac{2n}{n-2}.$$

But in Theorem 2

$$\rho \leq \frac{2}{n-2} \Rightarrow \rho n \leq \frac{2n}{n-2} = q \Rightarrow \rho n \leq q.$$

We have

$$H_0^1(\Omega) \subset L^q(\Omega), \quad \frac{1}{q} = \frac{1}{2} - \frac{1}{n}, n \geq 3$$

Then

$$\left| \int_\Omega \left(|u|^\rho u - |v|^\rho v \right) \Psi(t) \, dx \right| \leq .$$

$$c \left(\|u(t)\|^\rho + \|v(t)\|^\rho \right) \left(\|w_1(t)\|_{L^q(\Omega)} + \|w_1(s)\|_{L^q(\Omega)} \right) \|w(t)\|_{L^2(\Omega)}$$

And as $u, v \in L^\infty\left(0, T; H_0^1(\Omega)\right)$ for $\left(H_0^1(\Omega) \subset L^q(\Omega) \right)$, we have :

$$\left| \int_\Omega \left(|u|^\rho u - |v|^\rho v \right) \Psi(t) \, dx \right| \leq c \, |w(t)| \left(\|w_1(t)\| + \|w_1(s)\| \right).$$

So

$$|w(s)|^2 + \|w_1(s)\|^2 \leq c \int_0^s \left(|w(t)|^2 + \|w_1(t)\|^2 \right) dt.$$

According to Gronwall inequality we have:

$$|w(s)|^2 + \|w_1(s)\|^2 = 0 \Rightarrow$$

$$\begin{cases} w(s) = 0 \\ w_1(s) = 0 \end{cases} \Rightarrow u = v.$$

Then we have the uniqueness.

References

[1] R.A. Adams, Sobolev Spaces, Academic Press, (1976).

[2] H. Brezis, Analyse fonctionnelle, théorie et applications. Masson (1983).

[3] H. Brezis, Equations et inéquations non linéaires dans les espaces vectoriels en dualité, Ann, Ins.Fourier; 18, (1968), 115-175.

[4] G. Duvaut, J.L. Lions, Les inéquations en mécanique et en physique. Dunod. Paris. (1972).

[5] J.L. Lions, Quelques méthodes de résolution des problèmes aux limites non linéaires. Dunod. (1969).

[6] Luc Tartar, Topics in non lineair analysis. Université de Paris-Sud, Publications Mathematiques d'Orsay,novembre (1978).

[7] M.Meflah, A Similar Nonlinear Telegraph Problem Governed by Lamé System, International journal of Nonlinear Science (2012), ISSN: 2241-0503

[8] M.Meflah, Periodic Solution of A Nonlinear Problem by Elliptic Regularization Techniques, J. Math. Comput. Sci. 2(2012),No. 4,1078 -1085, ISSN: 1926-5307

[9] M.Meflah, Study of Nonlinear Elasticity Problem by Elliptic Regularization with Lamé System, Int. J. of. Mathematical Archive-2(5), May 2011 Page 693-697, ISSN 2229-5046

[10] M. Meflah, A Nonlinear Elasticity Problem by Elliptic Regularization Technics, Int. J. Contemp. Math. Sciences, Vol 6, 2011,no. 25, 1221-1229

[11] M. Meflah, B. Merouani, A Nonlinear Elasticity Problem Governed by Lamé System, Applied Mathematical Sciences, Vol.4, 2010,no. 36,1785-1796.

[12] F. Messelmi, B. Merouani, M. Meflah, Nonlinear thermoelasticity problem, Analele Universitatii Oradea, Fasc. Matematica,Tom XV (2008), 207-217.

[13] V. Patron, P. Perline, Méthode de la théorie mathématique de l'élasticité, Editions Mir, Moscou, 1981.

Universal fractal time of biological growth

Marcin Molski

Department of Theoretical Chemistry
Adam Mickiewicz University of Poznań
ul. Grunwaldzka 6, PL 60-780 Poznań, Poland
E-mail: mamolski@amu.edu.pl

Abstract: The West-Brown-Enquist universal growth curve has been mapped on the power law function with the time-dependent scaling factor and exponent representing the temporal fractal dimension of the growth of species like mammals, birds, fish, crustaceans, regardless of taxon, cellular metabolic rate and body size. The results obtained permit formulation of three important rules governing the biological growth: (i) growing biological systems possess its own, internal, universal fractal time, which differs from the linear scalar time of the external observer, (ii) fractal structure of the universal time is lost during growth, (iii) the universal growth belongs to the class of macroscopic non-local quasi-quantum phenomena.

Keywords: Biological growth, Fractal time, Mapping method, Nonlocality, Quasi-quantum phenomena

1. Introduction

Recently, an idea has been developed that the growth curves describing neuronal differentiation [1] or malignant tumour progression [2] can be successfully fitted by the fractal function

$$y(t) = a_t(t)t^{b_t(t)} \tag{1}$$

with the scaling factor $a_t(t)$ and exponent $b_t(t)$ as the functions of time. The formula (1) is derived by the mapping the sigmoidal Gompertz function [3]

$$G(t) = G_0 e^{\frac{b}{a}\left(1-e^{-at}\right)} \tag{2}$$

widely used to describe the time-evolution of the biological system (organism, organ, tissue, bacterial colony, tumour etc.) on the power one. In this approach we employ the generalized spline interpolation method [4], which permits interpolating the Gompertz function (2) by a family of power law curves

$$\left\{ y_i(t) = a_t(t_i)t^{b_t(t_i)} + y_0 \quad i = 1, 2, \dots N \right\} \tag{3}$$

determined at the points $\{t_i, y_i(t_i)\}$. Defining the sets of parameters $a_t = \{a_t(t_i), i=1,2\dots\}$, $b_t = \{b_t(t_i), i=1,2\dots\}$, one may derive the fractal function (1) assuming that functions (2) and (3) are isovalued and isosloped for the each moment of time. In such circumstances the equality of the functions (2) and (3) as well as their first derivatives provides the set of equations [1,2]

$$b_t(t) = bte^{-at} \frac{e^{\frac{b}{a}\left(1-e^{-at}\right)}}{e^{\frac{b}{a}\left(1-e^{-at}\right)} - 1} \qquad a_t(t) = t^{-b_t} G_0 \left[e^{\frac{b}{a}\left(1-e^{-at}\right)} - 1 \right] \qquad (4)$$

Here, G_0 stands for the initial mass, volume, diameter or number of proliferating cells, a - is the retardation constant whereas b denotes the initial growth or regression rate constant.

The main objective of the present study is extension of the research area on the ontogenic growth described by the West-Brown-Enquist function [5]

$$m(t) = M \left[1 - c_0 \exp(-c_1 t) \right]^{\frac{1}{c_2}} \qquad (5)$$

derived from the first principles: the conservation of metabolic energy, the allometric scaling of metabolic rate, energetic costs of producing and maintaining biomass. In the above formulae

$$c_0 = 1 - \left(\frac{m_0}{M} \right)^{1/4} \quad c_1 = \frac{a}{4M^{1/4}} \quad c_2 = \frac{1}{4} \quad M = m(t = \infty) \quad m_0 = m(t = 0) \quad (6)$$

m_0 denotes the initial mass of the system, M is the maximum body size reached whereas a is the metabolic parameter. The function (5) can be expressed in dimensionless form

$$r(\tau) = \left[\frac{m(t)}{M} \right]^{1/4} = 1 - \exp(-\tau) \qquad \tau = c_1 t - \ln(c_0) \qquad (7)$$

which has been named the *universal growth function* [5]. It almost perfectly describes the growth of all known species like mammals, birds, fish, crustaceans, regardless of taxon, cellular metabolic rate and body size [5].

Recently, the West-Brown-Enquist model has been successfully applied to fit the data for the different types of the tumours [6]. In particular, it has been demonstrated [7] that instead of the function (7) its generalized form

$$R(\tau) = \left[\frac{m(t)}{M} \right]^{1-p} = 1 - \exp(-\tau) \qquad \tau = (1-p)c_1 t - \ln(c_0) \qquad (8)$$

$$c_0 = 1 - \left(\frac{m_0}{M} \right)^{1-p} \quad c_1 = aM^{p-1} \quad c_2 = 1 - p \qquad (9)$$

better reproduces the tumor growth than the original function (5). Here, parameter p takes the value in the range<2/3, 1> [7]. Hence, the both universal growth functions (7) and (8) can be applied as input for the mapping procedure to obtain the fractal function (1) characterizing the growth of the species like mammals, birds, fish, crustaceans and different kinds of tumors.

The main purpose of the present work is mapping the functions (7) and (8) on the power law one using the spline interpolation method outlined above. As the result one gets the time-dependent universal fractal dimension $b_\tau(\tau)$ and the scaling factor $a_\tau(\tau)$ appearing in generalized τ-dependent function (1), which includes universal time τ instead of t. The analytical formulae $b_\tau(\tau)$ and $a_\tau(\tau)$ will

be employed to calculate their values at an arbitrary moment of time and to interpret the biological growth in the terms of the quasi-quantum model of life [8].

2. The Method

The West et al. [5] universal curve representing the growth of different biological species is employed to formulate the model considered here and to derive the universal power law function describing the biological growth in the space-time with universal temporal fractal dimension. All operations (plotting, integration, differentiation) were performed by making use of a Maple vs.14 processor for symbolic calculations. To avoid errors, the derivation of the mathematical formulae was also carried out by the Maple software. Proceeding along the line of the generalized spline interpolation method outlined above, the universal growth function (7) can be converted into power law using the set of nonlinear equations

$$a_\tau \tau^{b_\tau} = 1 - \exp(-\tau) \qquad b_\tau a_\tau \tau^{b_\tau - 1} = \exp(-\tau) \tag{10}$$

which assume that power law (3) and the universal growth (7) functions are isovalued and isosloped for the each moment of the universal time. The solution of the nonlinear set of equations (8) is the universal fractal dimension and the scaling factor

$$b_\tau(\tau) = \frac{\tau \exp(-\tau)}{1 - \exp(-\tau)} \qquad a_\tau(\tau) = \tau^{-b_\tau} \left[1 - \exp(-\tau) \right] \tag{11}$$

which define the universal fractal function

$$y(\tau) = a_\tau(\tau) \tau^{b_\tau(\tau)} \tag{12}$$

describing the biological growth in the space-time with the universal time τ defined by (7). The equation (10) permits formulating the power law function governing the growth of all species, independently of their biological characteristics, e.g. a, M and m_0. The plots of the universal fractal dimension $b_\tau(\tau)$ and scaling factor $a_\tau(\tau)$ generated from (9) are presented in Fig. 1.
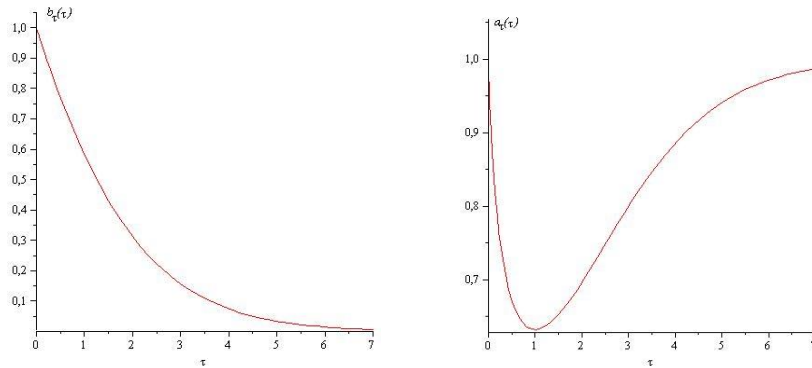
Fig. 1. The universal fractal dimension $b_\tau(\tau)$ and scaling factor $a_\tau(\tau)$ generated from Eqs. (11).

One may prove that the universal growth function (8) satisfies the first- and second-order differential equations

$$\frac{d}{d\tau}R(\tau) - \frac{\exp(-\tau)}{1-\exp(-\tau)}R(\tau) = 0, \frac{d^2}{d\tau^2}R(\tau) + \frac{\exp(-\tau)}{1-\exp(-\tau)}R(\tau) = 0 \quad (13)$$

The second term in the above equations represents the well-known in the quantum physics Hulthèn potential [9] widely used in description of the electrostatic interactions between micro-particles. One may prove that this equation is a special case of the quantal non-local Horodecki-Feinberg equation [10,11] for the time-dependent Hulthèn potential [9]

$$\frac{d^2}{d\tau^2}\Psi_v + \beta^2 \frac{\exp[-\tau]}{1-\exp[-\tau]}\Psi_v = \varepsilon_v^2\Psi_v \quad \varepsilon_v = \frac{\beta^2-v^2}{2\beta v} \quad v=1,2... \quad (14)$$

$$\beta^2 = \frac{2mc^2V_0}{\hbar^2 c_1^2} \qquad \varepsilon_v^2 = -\frac{2mc^3P_v}{\hbar^2 c_1^2}$$

$$\Psi_v = \exp(-\varepsilon\tau)\left[1-\exp(-\tau)\right]_2 F_1[2\varepsilon_v+1+v,1-v,2\varepsilon_v+1;\exp(-\tau)]$$

For the *critical screening* [12] (β=1) and ground quantum state (v=1) the quantum wave function Ψ_1 reduces to the macroscopic growth function $R(\tau)$

$$\Psi_1 = \left[1-\exp(-\tau)\right]\exp(-\varepsilon_1\tau) \xrightarrow{\beta=1,\varepsilon_1=0} R(\tau) = 1-\exp(-\tau) \quad (15)$$

This result indicates that the biological growth according to the universal growth function (8) belongs to the class of macroscopic non-local quasi-quantum phenomena. The notion *quasi-quantum* refers to the possibility of application of the quantum language and formalism in description of macroscopic objects [8] as this equation does not contain the Planck's constant and is a special case of the quantal Horodecki-Feinberg equation.

3. Conclusions

The calculations performed reveal that the fractal dimension $b_\tau(\tau)$ decreases to zero from the maximum value equal to one. On the contrary, the scaling factor at the beginning takes the value one $a_\tau(\tau=0)=1$ and then decreases to 0.6321 for $\tau=1$ (it corresponds to $b_\tau(\tau=1)=0.5820$); then it tends to the asymptotic value equal to one $a_\tau(\tau\rightarrow\infty)=1$. The results obtained permit formulation of three interesting rules governing the biological growth in the space-time with universal time τ, from which the first two conform acceptably with the results of our previous investigation on the neuronal differentiation and tumorigenessis [1,2]:

(i)   Growth of biological systems according to the universal West et al. function (8) can be described in the space-time with internal

universal fractal time, which differs from the linear $b_\tau(\tau=0)=1$ scalar time of the external observer.

(ii) Fractal structure of the universal time is lost during biological growth.

(iii) Universal growth belongs to the class of macroscopic non-local quasi-quantum phenomena.

As far as point (i) is concerned, if we assume that time is a continuous variable, it is clear that at the beginning of growth of a biological system it takes place in the space-time with the temporal fractal dimension $b_\tau(\tau=0)=1$ equal to the extrasystemic (physical) time. During growth, it is continuously transformed into intrasystemic universal fractal time, which diminishes to zero as growth continues.

References

1. M. Molski and J. Konarski. Neuronal differentiation and synapse formation in the space-time with temporal fractal dimension. *Synapse* 60: 567-72, 2006.

2. M. Molski and J. Konarski. Tumor growth in the space-time with temporal fractal dimension. *Chaos, Solitons & Fractals* 36: 811-18, 2008.

3. B. Gompertz On the nature of the function expressive of the law of human mortality, and on a new mode of determining the value of life contingencies. *Phil Trans Roy Soc London* 115:513-85, 1825.

4. B.D. Bojanov, H.A. Hakopian, A.A. Sahakian. *Spline functions and multivariate interpolations*. Springer-Verlag Gmbh 1993.

5. G.B. West, J.H. Brown, B.J. Enquist. A general model for ontogenic growth. *Nature*. 413: 628-31, 2001.

6. C. Guiot, .G. Degiorgis, P.P. Delsanoto, P. Gabriele, T.S. Deisboeck. *J. Theor. Biol.* 225: 147: 151-59, 2003.

7. C. Guiot, P.P. Delsanto, A. Carpinteri, N. Pugno, Y. Mansury, T.C. Deisboec. The dynamical evolution of the power exponent in a universal growth model of tumors. *J. Theor. Biol*. 240:459-63, 2006.

8. M. Molski. Living systems as coherent anharmonic oscillators. *Journal of Physics Conf. Ser*. 329: 012010, 2011.

9. L. Hulthén. Über die Eigenlösungen der Schrödingergleichung des Deuterons Ark. *Mat. Astron. Fys.* A. 28: 1–12, 1942.

10. G. Feinberg. Possibility of faster-than-light particles. *Physical Review*. 159:1089 – 1105, 1967.

11. R. Horodecki R. Extended wave description of a massive spin-0 particles, *Il Nuovo Cimento* B 102: 27–32, 1988.

12. Y.P. Varshni. Eigenenergies and oscillator strengths for the Hulthén potential. *Physical Review* A. 41, 4682-88, 1990.

Performance Analysis of Chaotic TH-CDMA for UWB Impulse Radio Communications

Anis Naanaa

Sys'com Laboratory, National Engineering School of Tunis (ENIT), Tunisia.
(E-mail: anis_naanaa@yahoo.com)

Abstract. In presence of Multiple User Interference (MUI), the performance of Impulse Radio Ultra Wide Band (IR-UWB) system is deteriorated. Hence the choice of codes allowing multiple access is crucial for minimizing the MUI and for enhancing the system performance. In this paper, we tackle the Bit Error Rate (BER) performance analysis of Chaotic Time Hopping (Chaotic-TH) UWB employing Pulse Position Modulation (PPM). Under this assumption, we derive an exact expression for the BER based on the UWB indoor communication with Line Of Sight (LOS) multipath channel. Computer simulation results have shown that the proposed Skew Tent Map (STM) Chaotic-TH sequences outperforms the conventional code based Gold sequences.

Keywords: Chaotic Time Hopping Code, Ultra Wide Band, Pulse Position Modulation, Bit Error Rate.

1   Introduction

Recently, research activities have focused on utilizing Ultra Wide Band (UWB) system for wide exploitation such as tracking applications, precision locating, wireless and sensor data collection, Ad Hoc and commercial applications [1]. UWB supporting its coexistence with overlapping spectrum technologies (other narrow and wide band wireless systems), offers promises to satisfy the requirements of low cost and high-speed digital home networks and reducing the multipath.

TH combined with PPM was originally proposed for UWB systems [1,2]. Currently, TH-PPM and TH-BPSK UWB systems are often considered as alternatives for a given application, although the differences between the two systems lead to different performance characteristics. This is due to the fact that pulse-position modulation (PPM) is habitually adopted in UWB systems, a modulation format that is characterized by conveying the information message on the time position of the transmitted pulses. Since UWB transmitted pulses have an extremely short time duration.

Despite of the increasing interest in UWB technology, there are still several challenging issues to be addressed regarding the signal processing at the receiver [3]. Probably the most critical aspect is the multi-user interference, modulation type and the codes allowing multiple access of UWB systems. Thus, the choice

of criteria is prominent for enhancement the performance of UWB systems.

Different methods have been proposed in the recent past for evaluating the effect of MUI on the performance of UWB systems. Recently the research has been focused on the statistical characteristics of the MUI. Many of them have modeled the MUI as a standard Gaussian approximation (SGA) [2,4,5].
Other works have dealt with the optimization of the performance by code selection [6–8]. In [9], MUI was modeled based on the observation that interference in UWB system is provoked by collisions occurring between pulses belonging to different transmissions.

The novelty of this work is to propose a code optimization method to minimize collisions with other users. The idea consists to combined Time Hopping with Code Division Multiple Access (TH-CDMA) such as in cellular network. A novel analytical expression is derived, inspired from the Developed Time Hopping Codes (DTHC), originally introduced in [10]. This results is established in the case of Impulse Radio (IR)-UWB signals employing PPM modulation in combination with TH-code (THC), and propagation over realistic channel IEEE 802.15.4a indoor communication CM1 [11].

The rest of this paper is organized as follows Section 2 the TH-UWB system model is presented. In section 3, we describe briefly, the THC using in this paper such as Gold sequences and STM sequences. Thereafter we propose a code optimization method to minimize the number of collisions in Time Hopping-Code Division Multiple Access (TH-CDMA). In section 4, we compare our method with THC. The efficiency of TH-CDMA is verified by simulation results. On the other hand, chaotic sequences outperforms Gold sequences in term of BER. Finally, conclusions appear in section 5.

2   IR-UWB signal model

In this work we focus on the design of an asynchronous UWB-IR system when multi user make a non-coordinated usage of the same bandwidth. In this scenario the overall performance is dominated by the MUI and a TH sequence is assigned to each user in order to reduce the overall interference that arises from collision with other users transmission.
The block diagram of the system model is described in Fig. 1. Subsequently, we give the transmitted signal model for PPM modulation, the channel model and the correlating receiver structure. Then we develop the variance expression of the MUI for the PPM modulation.
.

In summary, when multiple access is affected by using THC, the resulting signal $s_{tr}^{(j)}(t)$ corresponding to N_u users in a TH-UWB system, with equiprobable data $b^{(j)} \in [0\ 1]$ mapped through binary PPM with the time shift δ set to
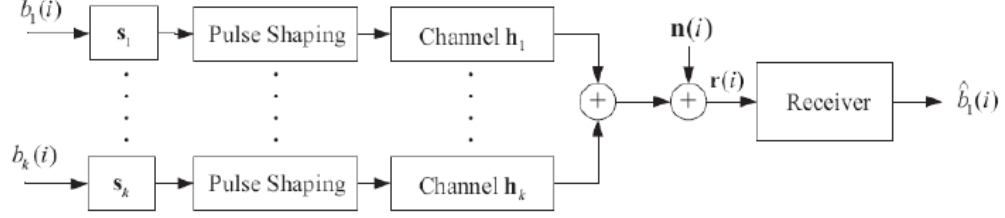
Fig. 1. Block diagram of the TH-PPM-UWB signal.

equal the pulse width, is given by [1]:

$$s_{tr}^{(j)}(t) = \sqrt{\frac{E_b^{(j)}}{N_f}} \sum_{k=-\infty}^{\infty} w(t - kT_f - \widetilde{c}_k^{(j)}T_c - b_{\lfloor k/N_f \rfloor}^{(j)}\delta - \theta_j) \tag{1}$$

Where $E_b^{(j)}$ is the received symbol energy for the jth user, N_f is the number of pulses transmitted for each bit. $w(t)$ represents pulse shaping with pulse width τ, T_f is the frame time, each frame has a duration of T_f. Each frame divided into N_c time chips, each time chip has a duration of T_c. $\widetilde{c}_k^{(j)}$ represents the THC sequence assigned to j^{th} user, will be modeled as independent random variables and are assumed to be periodic of period N_f. $\widetilde{c}_k^{(j)}$ taking values in $[0, N_c - 1]$ with equal probability. Therefore the THC sequence provides an additional shift (in multiples of the chip time T_c), in order to reduce collisions effects in multiple access. $\lfloor . \rfloor$ is the floor operator and $b_k^{(j)} \in \{0, 1\}$ is the binary sequence of the transmitted symbol at time k corresponding to user j supposed to be independent and identically distributed. δ is the time shift associated with binary PPM that is, the pulses corresponding to bit 1 are sent δ seconds later than the pulses corresponding to bit 0. θ_j accounts for the asynchronism between the different users and will be assumed to be uniformly distributed.

A typical pulse employed in the literature [1,2] is the second derivative of a Gaussian pulse has the form

$$w(t) = (1 - 4\pi(\frac{t}{\tau})^2) \exp(-2\pi(\frac{t}{\tau})^2) \tag{2}$$

According to the model proposed by the IEEE 802.15.4a working group [11] the channel impulse response is written as

$$h^{(j)}(t) = \sum_{m=0}^{M_p-1} \sum_{r=0}^{R-1} \alpha_{r,m}^{(j)}\delta(t - T_m^{(j)} - \tau_{r,m}^{(j)}) \tag{3}$$

where M_p is the number of multipath components, R is the number of rays, $\alpha_{r,m}$ is the tap weight of the rth ray (path) in the mth cluster each users may experience different number of propagation paths, δ is the Dirac delta function. T_m is arrival time of the mth cluster and $\tau_{r,m}$ is the arrival time of the rth ray relative to the mth cluster. By definition, $\tau_{0,m} = 0$.

The cluster arrival time is modeled as a Poisson process and the ray arrival time is modeled as a mixed Poisson process in [11].

The parameters of the channel as a function of the transmitter-receiver distance and the LOS availability. The value of the parameters are given in table 1.

Table 1. IEEE 802.15.4a Channel parameters CM1

Target Channel Characteristics	CM1
Λ (ns^{-1})	0.047
Distance (m)	$7 - 20$
Line of Sight	Yes
β is the mixture probability	0.095
λ_1 Ray arrival rate for mixture of poisson processes (ns^{-1})	1.54
λ_2 Ray arrival rate for mixture of poisson processes (ns^{-1})	0.15
m_0 Mean of log-normal distributed nakagami-m factor (dB)	0.67
$\widehat{m}_0$ Standard deviation of log-normal distributed nakagami-m factor (dB)	0.28

Assuming N_u users transmitting asynchronously, then we can write the received signal as

$$r(t) = \sum_{j=1}^{N_u} s_{tr}^{(j)}(t) * h^{(j)}(t) + n(t) \tag{4}$$

where each signal $s_{tr}^{(j)}(t)$ experiences a different multipath channel $h^{(j)}(t)$ that accounts for fading and delays from j^{th} user to the reference one. $*$ denotes the convolution operator, $n(t)$ is an Additive White Gaussian Noise (AWGN) process with zero mean and variance $E\{n(t)\} = N_0/2$ for each t. The impulse response in CM1 channel is depicted in figure 2.

The output of the correlating receiver of the ith user at time T_h is given by:

$$s_{rec}^{(i)}(T_h) = \sum_{p=0}^{N_f-1} \int_{T_h T_s + pT_f + \widetilde{c}_p^{(i)} T_c + \tau_{0,0}^{(i)} + T_0^{(i)}}^{T_h T_s + pT_f + \widetilde{c}_p^{(i)} T_c + T_c + \tau_{0,0}^{(i)} + T_0^{(i)}} r(t) v(t - T_h T_s - pT_f - \widetilde{c}_p^{(i)} T_c - \tau_{0,0}^{(i)} - T_0^{(i)}) dt \tag{5}$$

where $v(t)$ is the receiver's template signal defined by $v(t) = w(t+\delta) - w(t)$. An accurate value of $\tau_{0,0}^{(i)}$ can be obtained by UWB acquisition techniques. From the previous equations and after variable changes, we obtain

$$s_{rec}^{(i)}(T_h) = T_U(i) + T_{ISI}(i) + T_I(i) + T_N(i) \tag{6}$$

with

$$T_U(i) = \sum_{p=0}^{N_f-1} \alpha_{0,0}^{(i)} \int_0^{T_c} s_{tr}^{(i)}(t + T_h T_s + pT_f + \widetilde{c}_p^{(i)} T_c) v(t) dt$$

$$T_{ISI}(i) = \sum_{p=0}^{N_f-1} \sum_{m=0}^{M_p-1} \sum_{r=0, r+m \neq 0}^{R-1} \alpha_{r,m}^{(i)} \int_0^{T_c} s_{tr}^{(i)}(t + T_h T_s + pT_f + \widetilde{c}_p^{(i)} T_c + T_0^{(i)} - T_m^{(i)} + \tau_{0,0}^{(i)} - \tau_{r,m}^{(i)}) v(t) dt$$
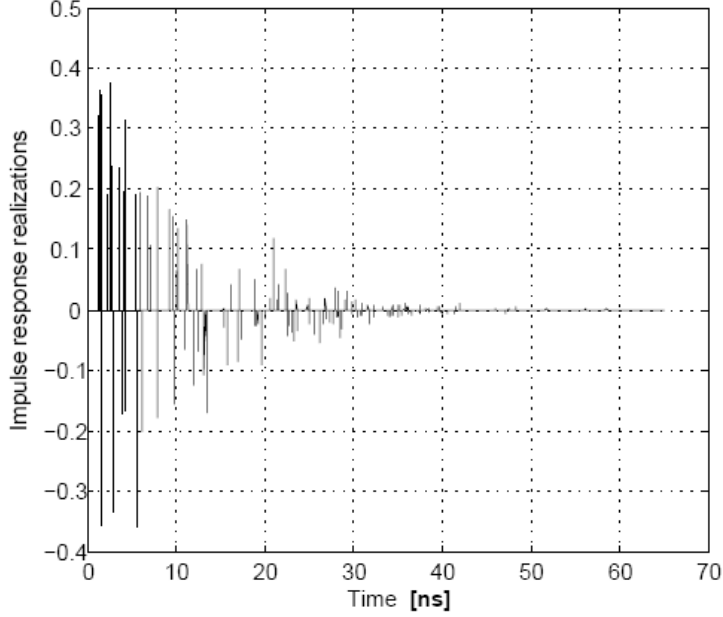
Fig. 2. One realization of UWB channel model CM1.

$$T_I(i) = \sum_{p=0}^{N_f-1} \sum_{m=0}^{M_p-1} \sum_{r=0}^{R-1} \alpha_{r,m}^{(j)} \int_0^{T_c} \sum_{j=1, j \neq i}^{N_u} s_{tr}^{(j)}(t + T_h T_s + pT_f + \widetilde{c}_p^{(i)} T_c + T_0^{(i)} - T_m^{(j)} + \tau_{0,0}^{(i)} - \tau_{r,m}^{(j)}) v(t) dt$$

$$T_N(i) = \sum_{p=0}^{N_f-1} \int_0^{T_c} n(t) v(t) dt$$

T_U is the useful signal, T_{ISI} is inter-symbol interference signal, T_I is the MUI and T_N is the term corresponding to the noise.

In [12], we defined a criterion named ACN for selecting code sequences in synchronous and single-path TH-UWB system. Also we showed numerically, that this criterion is adequate even in the multipath channel case. Indeed in the synchronous case, we showed that

$$T_I(i) = E_w \sum_{j=1, j \neq i}^{N_u} \alpha^{(j)} (2b_h^{(j)} - 1) cn(s_i, s_j) \tag{7}$$

where E_w is the amplitude which controls the transmitted power, $\alpha^{(j)}$ is the tap weight of the user j, $b_h^{(j)}$ is the binary sequence, $cn(s_i, s_j)$ is the number of collision between codes $\widetilde{c}^{(i)}$ and $\widetilde{c}^{(j)}$. $\widetilde{c}^{(j)}$ can be computed by taking into account the developed Time-Hopping Codes (DTHC) [10] corresponding to THC as follows: for a given code $\widetilde{c}_l^{(j)}$, the DTHC is a binary code of length

329

$N_c N_f$ and is defined by

$$c_r^{(j)} = \begin{cases} 1 \; \mathrm{i}f \; r = \widetilde{c}_l^{(j)} + lN_c, & r = 0\ldots, N_c N_f - 1. \\ 0 \; otherwise. & 0 \leq l \leq N_f - 1, \end{cases} \tag{8}$$

The relation between TH sequence $\widetilde{c}_l^{(j)}$ and the developed code $c_r^{(j)}$ is illustrated by an example in Fig. 3 and given by the following equation according to equation (7).
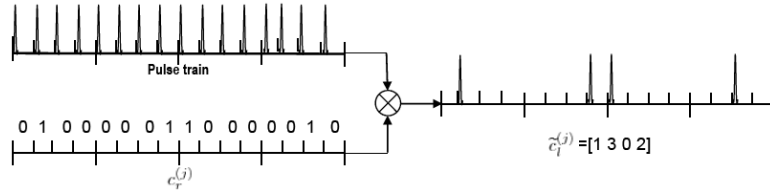

Fig. 3. DTHC corresponding to the THC [1 3 0 2].

$$cn(i,j) = \sum_{l=0}^{N_f N_c - 1} c_l^{(i)} c_l^{(j)} \tag{9}$$

The Average Collision Number ACN of the sequence set $\widetilde{c}^{(j)}$, $j = 1, \ldots N_u$ is therefore defined by [12]:

$$ASCN = \frac{1}{N_u(N_u - 1)} \sum_{i=1}^{N_u} \sum_{j=1, j \neq i}^{N_u} cn^2(i,j) \tag{10}$$

3   The proposed codes

In this section we begin by present the THC using in this paper such as Gold sequences and STM sequences. Thereafter we propose a code optimization method to reduce collisions with other users in Time Hopping-Code Division Multiple Access (TH-CDMA).

The Gold sequence based THC [12], taking values in $\{0, 1, \cdots, N_c - 1\}$. For $N_c = 16$ the THC takes values in $0 \leq \widetilde{c}_l^{(j)} \leq N_c - 1$ and is obtained by converting every k consecutive bits into a decimal in each row. k is given by $N_c = 2^k$.

Chaotic sequences have some properties that motivate researchers to use them in various applications. These properties are determinism, long term unpredictability and high sensitivity to initial conditions. Especially chaotic sequences generated by one dimensional non linear transformation have been used in cryptography, watermarking, spectrum spreading systems [13]. A non linear one dimensional discrete system is defined by

$$x_{k+1} = f_a(x_k) \tag{11}$$

where f_a is a parametric non linear transformation and a is called bifurcation parameter. The behavior of the system is determined by the Lyapunov exponent defined by

$$\lambda = \lim_{T \to +\infty} \frac{1}{T} \sum_{i=0}^{T-1} \ln |f_a'(x_i)| \tag{12}$$

If λ is positive the behavior of the system is chaotic, if it is negative the behavior is regular.

In this work we consider chaotic sequences STM defines as follows.

$$x_{n+1} = \begin{cases} \frac{x_n}{r}, & 0 \le x_n \le r \\ \frac{1-x_n}{1-r}, & r < x_n \le 1 \end{cases} \tag{13}$$

STM exhibits chaotic behavior for every value of the bifurcation parameter $r \in [0\ 1]$. The TH-codes are generated by quantization of the so generated sequences as follows:

$$q(x) = \lfloor x_{n+1} N_c \rfloor$$

$\lfloor . \rfloor$ is the floor operator.
Figure 4 show the Lyapunov exponent and ASCN versus the bifurcation parameter r for STM. We can see that the curves of the ASCN follow the one of Lyapunov exponent and that the greater the exponent is the smaller the ASCN. For $r = 0.5$, we have the best ASCN and Lyapuonv exponent. This example,
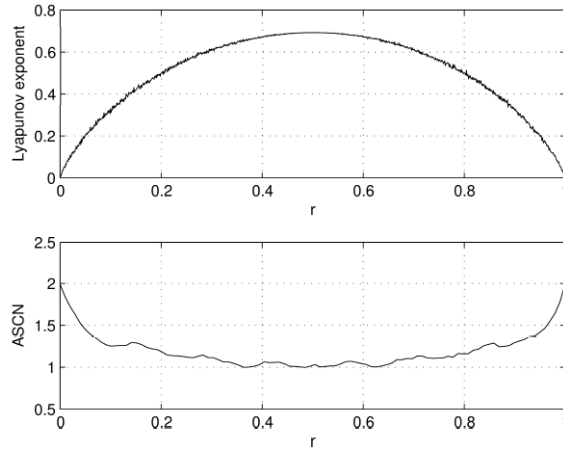
Fig. 4. Lyapunov exponent and ASCN for Skew tent map.

shows numerically that the ASCN of a quantized chaotic sequences depends on the chaoticity of these sequences measured by their Lyapunov exponent. All along this work we have taken $r = 0.5$.

In order to improve the performance of the TH-UWB system we present a novel construction code which have a fewest coincidences in their codes to get
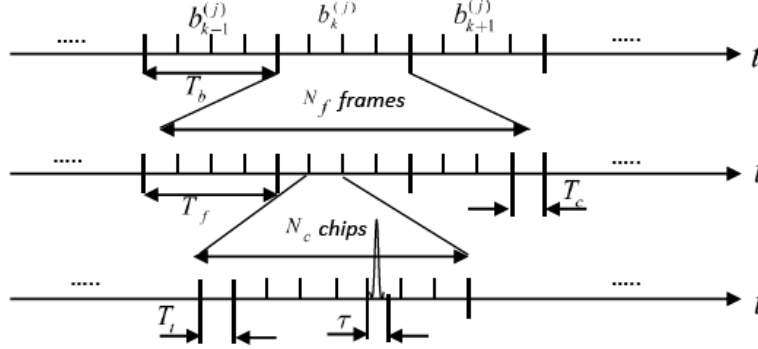
Fig. 5. Proposed TH-CDMA codes construction

the smaller ASCN. In figure 5, we have illustrated the proposed TH-CDMA codes wherein each frame divided into N_c time chips, each chip is divided into N_t slots. The pulses train are transmitted in every T_t. The code construction is given by the formula

$$\widetilde{c}_{TH}^{(j)} = N_t \widetilde{c}_l^{(j)} + \widetilde{c}_t^{(j)} + l N_t N_c \tag{14}$$

where $\widetilde{c}_l^{(j)}$ takes values in $[0, \ N_c - 1]$ and $\widetilde{c}_t^{(j)}$ takes values in $[0, \ N_t - 1]$, N_t is the time slots. $\widetilde{c}_l^{(j)}$ and $\widetilde{c}_t^{(j)}$ assigned to j^{th} user, will be modeled as independent random variables and are assumed to be periodic of period N_f. The parameter l take values in $0 \leq l \leq N_f - 1$.

In Fig. 6, we reported the ASCN versus the user number for $N_c = 16$. The STM are averaged over 100 realizations and the bifurcation parameter is set to the value that gives the best ASCN, i.e., $r = 0.5$. The initial inspection of the results reveals that the TH-CDMA sequences give a better ASCN than those of TH sequences. These results show the advantage of optimizing the code sequences for a TH-UWB system. Moreover, the results showed that STM have a better ASCN than Gold sequences. Furthermore, the results showed that when the number of users less than 7 ($N_u < 7$) in TH sequences and respectively when the number of users less than 10 users ($N_u < 10$) in TH-CDMA sequences, the ASCN obtained is zero. This explains that there is no collision. This is due to the fact that the Gold sequences are orthogonal for these values of N_u.

To see how these results are reflected on the performances of a TH-UWB-PPM system. In the next section, we evaluate the BER performance of TH-UWB-PPM using TH-CDMA sequences which is compared with THC sequences.

4 Simulation Results and Discussions

In the sequel, we consider the BER optimization of TH-UWB-PPM system in a residential environment CM1 channel by means of simulations. The simulation
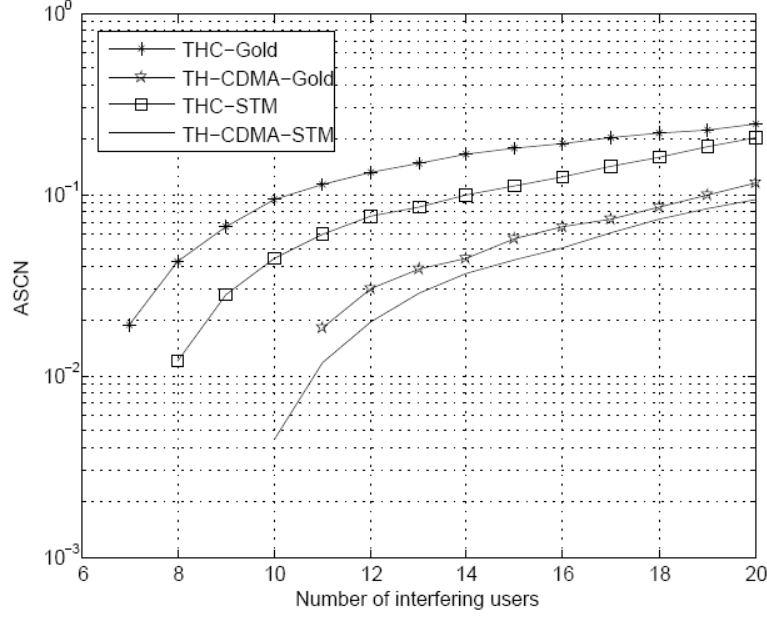
Fig. 6. ASCN versus user number in the asynchronous case for THC versus TH-CDMA Gold sequences

parameters are listed in Table 2. For simplicity, we will assume that the number of paths L is the same for all users.

Table 2. Major parameters of the TH-UWB system.

Simulation parameters	Acronym	Value
Chip duration	T_c	1ns
Pulse duration	τ	0.2ns
Number of slot	N_t	8
Number of chip	N_c	4,16
Number of path	L	10
Number of frame	N_f	4
Sampling frequency	F_s	8GHz
Number of sampling	N_e	50
Signal to Noise Ratio	SNR	10dB
Number of bits for each user	Nb	10^5
Factor for spread spectrum Gold	N	31

In Fig. 7, we have depicted the BER compared with the number of interfering users for THC versus TH-CDMA for both Gold and STM sequences. For $N_u < 10$, the BER is low and we did not find any error for a number of bit equal to 10^5.

We can see that TH-CDMA sequences have better performances than the THC

sequences. Likewise, we can see that the BER performances using chaotic sequences (STM) have better performance than classical sequences (Gold). Respectively for THC and TH-CDMA sequences.

These results validate the relevance of the ASCN as an 'off-line' performance evaluation criterion. Otherwise, if we use the classical sequences, we must transmit the code sequences for each user. On the other side, with chaotic sequences we just need to know the initial condition and the used chaotic map. This improves the quality and the security of the transmission, and shows the significance of using chaos in communication.
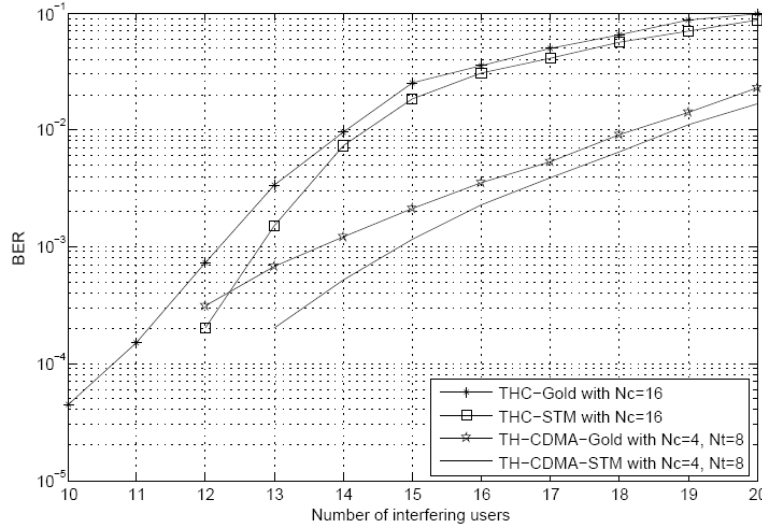
Fig. 7. BER versus user number for THC versus TH-CDMA Gold and STM sequences

5 Conclusion

In this paper, we studied the performance of a TH-UWB-PPM system in multiple access context. Due to the effect of the MUI on UWB systems, it is crucial to reduce the MUI in order to enhance the performance in term of bit error rate. Based on this observation, we proposed a simple method to optimize a code sequences called TH-CDMA. The UWB system using TH-CDMA code sequences show excellent attributes in terms of reduction of bit error rate compared to the THC and this is true for Gold and chaotic sequences (STM). The results shows the significance of using chaos in communication. We can also notice that the plots of the ASCN and the BER are highly correlated. Specifically, we showed that the higher the Lyapunov exponent is the lower is the ASCN. Which validate the use of the ASCN as an efficient off-line evaluation criterion.

References

1. M. L. Welborn, "System considerations for ultra-wideband wireless networks," *IEEE Radio and Wireless Conference*, pp. 5–8, (2001).
2. R. A. Scholtz, "Multiple Access with Time-Hopping Impulse Modulation," in *Proc. MILCOM 1993*, Bedford, MA, pp. 447–450, (1993).
3. L. Yang, and G. B. Giannakis, "Ultra-Wideband Communications: An idea whose time has come," *IEEE Signal Process. Mag.*, vol. 21, no. 6, pp. 26–54, (2004).
4. R. Tesi, J. Inatti, I. Oppermann, and V. Hovinen, "On the multi-user interference study for ultra wideband communication systems in AWGN and modified Saleh-Valenzuela channel," in *Proc. Int. Workshop of UWB Systems Joint with Conf. on UWB Systems and Technologies*, Kyoto, Japan, (2004).
5. A. Naanaa, S. Belghith "Performance Optimization of TH-UWB System in Multipath Channel," in *Int. Congress on Ultra Modern Telecommunications and Control Systems and Workshops, ICUMT*, Moscou, Russia, (2010).
6. C. Corrada Bravo, R. A. Scholtz, and P. V. Kumar, "Generating TH-SSMA sequences with good correlation and approximately flat PSD level," in *Proc. UWB Conf. on Radio and Radar Technology, Washington*, DC, USA, (1999).
7. O. Moreno, and S. V. Maric, "A new family of frequency hop codes", *IEEE Trans. Commun.*, vol. 48, pp. 1241–1244, (2000).
8. I. Guvenc, and H. Arslan, "Design and performance analysis of TH-sequences for UWB-IR systems," in *Proc. IEEE Wireless Communications and Networking Conf.*, Georgia, USA, pp. 914–919, (2004).
9. M. G. Di Benedetto, L. De Nardis, M. Junk, and G. Giancola, "$(UWB)^2$ Uncoordinated Wireless Baseborn Medium Access for UWB Communication Networks," *Mobile Networks and Applications*, vol. 10, pp. 663–674, (2005).
10. C. J. Le Martret and G. B. Giannakis, "All-Digital impulse radio for wireless cellular systems," *IEEE Trans On Comm*, vol. 50, no. 9, pp. 1440–1450, (2002).
11. Molisch, A.F., Balakrishnan, K., Cassioli, D., et al., "IEEE 802.15.4a channel model final report". *IEEE 802.15-04-0662-00-004a*, (2004).
12. A. Naanaa, S. Belghith "A combinatorial approach for enhancing the performance of TH-PPM UWB systems: chaotic vs. classical codes sequences," *Nonlinear Dynamics, Springer*, vol. 67, no. 2, pp. 1315–1326, (2012).
13. G.M. Maggio, N. RulLov and L. Rggiani, Pseudo chaotic time hopping for UWB impulse radio, *IEEE Trans. Circuits and Systems-I.*, vol. 48, No. 12, pp. 1424–1435, Dec. 2001.

Three-Dimensional Chaos Maps
and Fractal Sets with Physical Analogue

Nguyen Thanh Nhien[1], Dang Van Liet[2], and Shunji Kawamoto[3]

[1] Vietnam National University, University of Science, Ho Chi Minh City, Vietnam
  (E-mail: ntnhien@phys.hcmuns.edu.vn)
[2] Vietnam National University, University of Science, Ho Chi Minh City, Vietnam
  (E-mail: dangvanliet@phys.hcmuns.edu.vn)
[3] Osaka Prefecture University, Sakai, Osaka, Japan
  Vietnam National University, University of Science, Ho Chi Minh City, Vietnam
  (E-mail: kawamoto@eis.osakafu-u.ac.jp)

Abstract. A generalized logistic function is firstly introduced for the derivation of a generalized logistic map (GLM), which is shown to have generalized bifurcation diagrams, chaotic time series and fractal sets depending on the two real constants in the GLM. Next, a two-dimensional generalized chaos map without complex variables, which includes the Mandelbrot one as a special case, is constructed according to the structure of the GLM, and the fractal sets are discussed. Finally, it is concluded that the construction is expanded to a three-dimensional generalized chaos map based on three chaos solutions to the kernel map, and the fractal sets with physical analogue are numerically obtained.
Keywords: Chaos map, Fractal set, Logistic map, The Mandelbrot map, Bifurcation diagram, Three-dimensional simulation.

1 Introduction

For the study of dynamical systems, simple one-dimensional (1-D) nonlinear difference equations have arisen in the field of biological, economic and social sciences. A special example is the logistic map describing biological population growth, and the map possesses a rich spectrum of dynamical behavior which is called chaos in many respects [8, 9]. In particular, a bifurcation diagram of the two parameter quadratic family $x \rightarrow (x^2 - a)^2 - b$ has been observed [2], and the self-adjusting logistic map with a slowly changing parameter in time [10] and the logistic map with a periodically modulated parameter [14] have been considered. Moreover, coupled maps have been discussed for crises and hysteresis [3], wavelength doubling bifurcations [1], spatially coherent states [13], and the Mandelbrot set in electronic experiment [4].

On the other hand, fractals have been proposed and discussed for the geometric representation of shapes and irregular patterns in nature, and the concept of fractals has been useful for describing various natural objects, such as clouds, coasts, rivers and road networks [7]. However, it has been pointed out that the physics of fractals is a subject waiting to be born [5], since the Mandelbrot map has been defined as a complex map, and the map is known to be a special one in the sense of analytic complex function satisfying the Laplace equation [11].

In this paper, firstly we derive a 1-D generalized logistic map with two constants from a generalized logistic function for biological population growth. Noticing the structure of the 1-D map, we construct a two-dimensional (2-D) generalized Mandelbrot map and a three-dimensional (3-D) generalized chaos map. Finally, it is shown that

the 3-D map based on three chaos solutions to the kernel map has fractal sets with physical analogue, which are defined in the space of three initial values.

2 One-Dimensional Chaos Maps and Fractal Sets

We introduce here the logistic function $P(t)=1/(1+e^{-t})$ with the population growth $P(t)$ and the time $t>0$, which is applied to a range of fields including biology, demography, economics and probability. As a generalized logistic function, we treat the following one;

$$P(t) = \frac{a}{b + e^{-ct}} + d, \tag{1}$$

where coefficients $\{ a \neq 0, b > 0, c \neq 0, d \geq 0 \}$ are real constants, and d denotes a constant population growth term. From (1), we have the first order differential equation as;

$$\frac{dP}{dt} = (\frac{bc}{a})P\left[(\frac{a+2bd}{b}) - P\right] - (\frac{cd}{a})(a+bd). \tag{2}$$

Then, by the transformation

$$X \equiv P / \frac{(a+2bd)}{b}, \tag{3}$$

the discretization

$$\frac{dX}{dt} \equiv \frac{X_{n+1} - X_n}{\Delta t}, n = 0,1,2,\cdots, \tag{4}$$

and the transformation

$$x_n \equiv (B_0 / A) X_n, \tag{5}$$

where $\Delta t > 0$ is the time step, $A \equiv 1 + (\Delta t)\alpha$ and $B_0 \equiv (\Delta t)\alpha$ with $\alpha \equiv (c/a)(a+2bd),$ we find a 1-D generalized logistic map (GLM);

$$x_{n+1} = Ax_n(1 - x_n) + B, \tag{6}$$

here

$$A \equiv 1 + \frac{c(a+2bd)}{a}(\Delta t), \tag{7}$$

$$B \equiv \frac{-bc^2d(a+bd)(\Delta t)^2}{a[a+c(a+2bd)(\Delta t)]}. \tag{8}$$

If $d = 0$ in (7) and (8), then (6) gives a map $x_{n+1} = Ax_n(1 - x_n)$, which is the logistic

one, and the map at $A = 4.0$ has an exact chaos solution $x_n = \sin^2(C2^n)$ with a real constant $C \neq \pm m\pi/2^l$ and finite positive integers $\{l, m\}$, which has been applied to cryptosystems [6, 15], that is, we call the map $x_{n+1} = 4x_n(1 - x_n)$ the kernel map of (6). Therefore, the constant A in (6) denotes a coefficient of the nonlinear term, and the constant B corresponds to the constant population growth term d in (1). The constants A and B play a key role in the construction of 2-D and 3-D chaos maps in Sections 3 and 4.

The 1-D GLM derived as (6) gives, for example, the orbits in the case of (A, B) $=(3.0, 0.3)$ with the initial value $x_0 = 0.6$ as shown in Figure 1. In Figure 1, we illustrate the graph corresponding to the function $y = Ax(1 - x) + B$, which is a parabola depending on parameters A and B. The quadratic iteration is used here, and it is found that the orbits in Figure 1 do not always stay in the interval $[0, 1]$. Then, the generalized bifurcation diagrams depending on A and B of (6) are obtained as
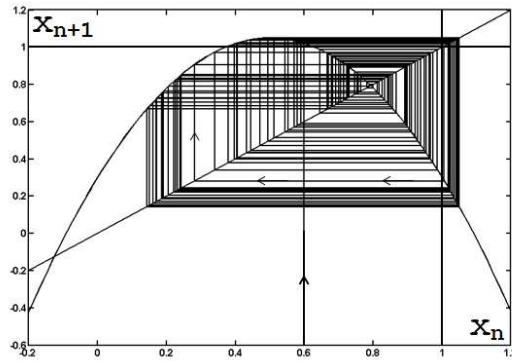
Fig. 1. A graphical iteration obtained by (6). The case of $(A, B) = (3.0, 0.3)$ and $x_0 = 0.6$ is shown.
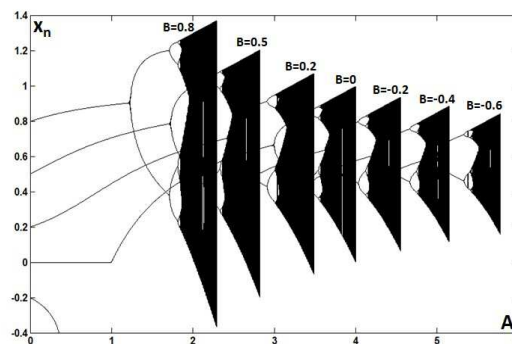
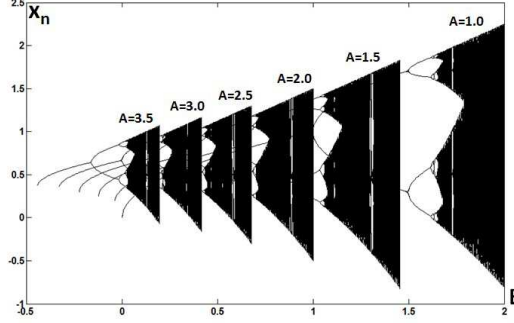Fig. 2. Generalized bifurcation diagrams in the case of the parameter B.

339

Fig. 3. Generalized bifurcation diagrams in the case of the parameter A.

presented in Figures 2 and 3 with $0 \leq A \leq 6.0$ and $-0.5 \leq B \leq 2.0$, respectively. The diagrams show plots of the asymptotic population numbers versus the parameter A or B, and the open areas or the windows in each diagram correspond to the area for periodic cycles as well discussed on the diagram for the logistic map. From the bifurcation diagrams of Figures 2 and 3, it is found that there exists a set defined as points of (A, B) on the A-B plane for which x_n in (6) does not go to infinity as $n \to \infty$. Here, since the set depends on parameters $\{A, B\}$, we treat the following set defined by

$$M_1 = \{A, B \in \mathbf{R} \mid \lim_{n \to \infty} x_n < \infty \}, \tag{9}$$

where x_n satisfies (6), and all the parameters are real numbers. In Figure 4(a), the set M_1 is obtained by iterating (6) with $x_0 = 0.6$. In Figure 4(a), the M_1 under $-4.0 \leq A \leq 4.0$ and $-10.0 \leq B \leq 10.0$ is shown. However, it should be noticed that the M_1 does not present a physical analogue because of a set on the A-B plane. If we zoom in near the point $(A, B) = (1.3416, 1.6574)$, then we find Figure 4(b). The same is true for other points, such as $(A, B) = (1.34146, 1.65724)$ and $(A, B) = (1.341434, 1.657167)$ in (c) and (d), respectively. Thus, there exists a self-similarity structure of open area in the M_1, that is, the M_1 has a fractal structure. The time series at points $\{P_1, P_2, P_3, P_4\}$ in Figure 4(a) are shown in Figure 5. All the time series in Figure 5 at the points in Figure 4(a) give chaotic behaviors, and the amplitude of time series corresponds proportionally to the value of B. Especially, it is found that the chaotic time series at points $\{P_1, P_2, P_3, P_4\}$ do not converge, and the fractal structure appears only in the first quadrant of Figure 4(a).

Similarly, according to the structure of (6), if we introduce an arbitrary chaos solution $x_n \equiv cf(n)$ to the kernel map $x_{n+1} \equiv g(x_n)$, we can construct the following 1-D generalized chaos map;

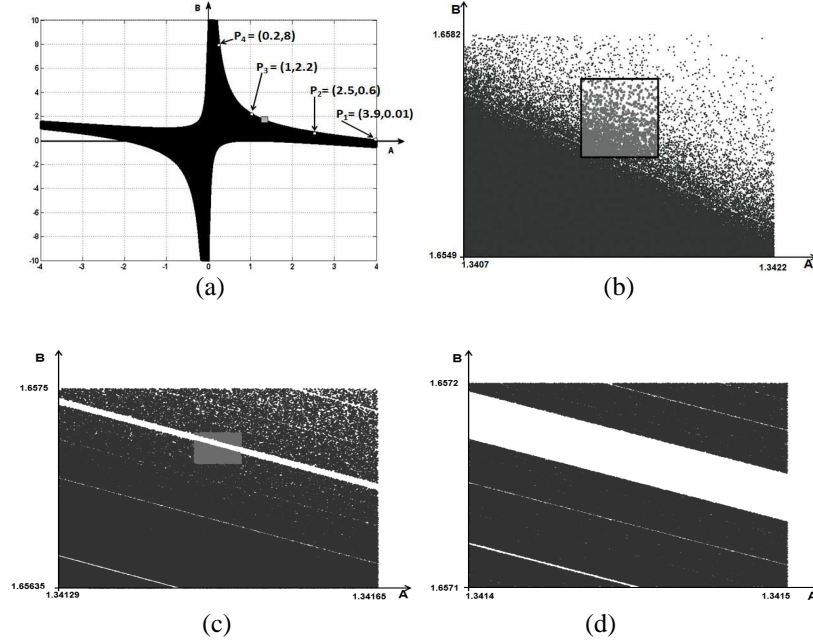$$x_{n+1} = Ag(x_n) + B \tag{10}$$

with real constants $\{A, B\}$.

Fig. 4. A set M_1 on the $A-B$ plane and the fractal structure. Figure (a) is a set under $-4.0 \le A \le 4.0$ and $-10.0 \le B \le 10.0$. Figures (b), (c) and (d) are the enlargements of the previous small framed region, respectively.
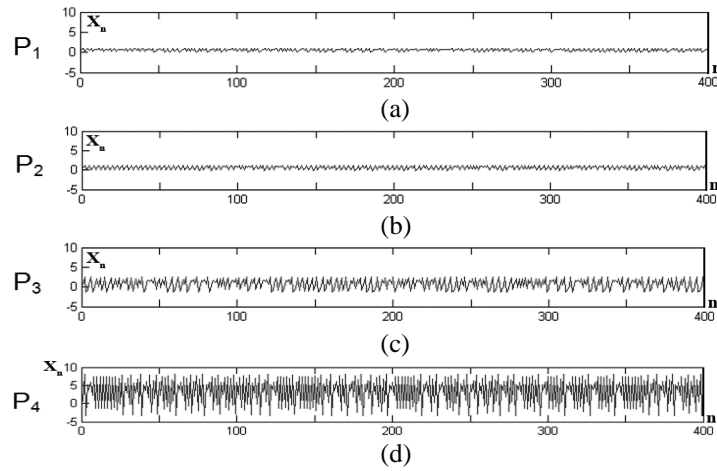

Fig. 5. Time series at points $\{P_1, P_2, P_3, P_4\}$ in Figure 4(a). The values of A and B in $(a)-(d)$ are $(A,B)=(3.9, 0.01), (2.5, 0.6),$ $(1.0, 2.2)$ and $(0.2, 8.0)$ at $\{P_1, P_2, P_3, P_4\}$, respectively.

341

3 Two-Dimensional Chaos Maps and Fractal Sets

As constructed in Section 2, we begin for 2-D chaos maps by setting two chaos solutions;

$$x_n = cf_1(n), \tag{11}$$

$$y_n = cf_2(n), \tag{12}$$

to the kernel map

$$x_{n+1} = g_1(x_n, y_n), \tag{13}$$

$$y_{n+1} = g_2(x_n, y_n), \tag{14}$$

and have a 2-D generalized chaos map as

$$x_{n+1} = a_1 g_1(x_n, y_n) + b_1, \tag{15}$$

$$y_{n+1} = a_2 g_2(x_n, y_n) + b_2, \tag{16}$$

where $\{a_1, a_2, b_1, b_2\}$ are real constants.

For example, from two chaos solutions $x_n = \cos(C2^n)$ and $y_n = \sin(C2^n)$ to the kernel map $x_{n+1} = (x_n^2 - y_n^2)$ and $y_{n+1} = 2x_n y_n$, we get a 2-D chaos map as

$$x_{n+1} = a_1(x_n^2 - y_n^2) + b_1, \tag{17}$$

$$y_{n+1} = a_2 x_n y_n + b_2. \tag{18}$$

Here, the case of $(b_1, b_2) = (x_0, y_0)$ or (k_1, k_2) is called M-type or J-type, respectively, where $\{x_0, y_0\}$ are initial values and $\{k_1, k_2\}$ are real constants, because the case of $(a_1, a_2, b_1, b_2) = (1.0, 2.0, x_0, y_0)$ gives the Mandelbrot map, and the case of $(a_1, a_2, b_1, b_2) = (1.0, 2.0, k_1, k_2)$ equals the Julia map derived from the complex map.

For the case of two chaos solutions;

$$x_n = \cos(C2^n), \tag{19}$$

$$y_n = \sin^2(C2^n), \tag{20}$$

to the kernel map $x_{n+1} = x_n^2 - y_n$ and $y_{n+1} = 4x_n^2 y_n$, we find the following 2-D generalized chaos map;

$$x_{n+1} = a_1(x_n^2 - y_n) + b_1, \tag{21}$$

$$y_{n+1} = a_2 x_n^2 y_n + b_2, \tag{22}$$

where the case of $(a_1, a_2, b_1, b_2) = (1.0, 4.0, x_0, y_0)$ or $(a_1, a_2, b_1, b_2) = (1.0, 4.0, k_1, k_2)$ yields a 2-D M-type or J-type chaos map, respectively. It is important to note

that the kernel map does not correspond to an analytic complex function satisfying the Laplace equation [11]. The fractal sets defined by

$$M_2 = \{x_0, y_0 \in \mathbf{R} \mid \lim_{n \to \infty} x_n, y_n < \infty\}, \tag{23}$$

are shown in Figures 6 and 7, here $\{x_0, y_0\}$ are initial values for the map (21) and (22). In Figure 6, the fractal structure has Holes in the set, and in Figure 7 the shape of the set gives a fractal one of Horn.

4 Three-Dimensional Chaos Maps and Fractal Sets

Then, for the construction of a 3-D generalized chaos map, we introduce three chaos solutions;

$$x_n = cf_1(n), \tag{24}$$

$$y_n = cf_2(n), \tag{25}$$

$$z_n = cf_3(n), \tag{26}$$

to the kernel map; $x_{n+1} = g_1(x_n, y_n, z_n)$, $y_{n+1} = g_2(x_n, y_n, z_n)$, $z_{n+1} = g_3(x_n, y_n, z_n)$. Thus, we obtain a 3-D generalized chaos map with three real coefficients $\{a_1, a_2, a_3\}$
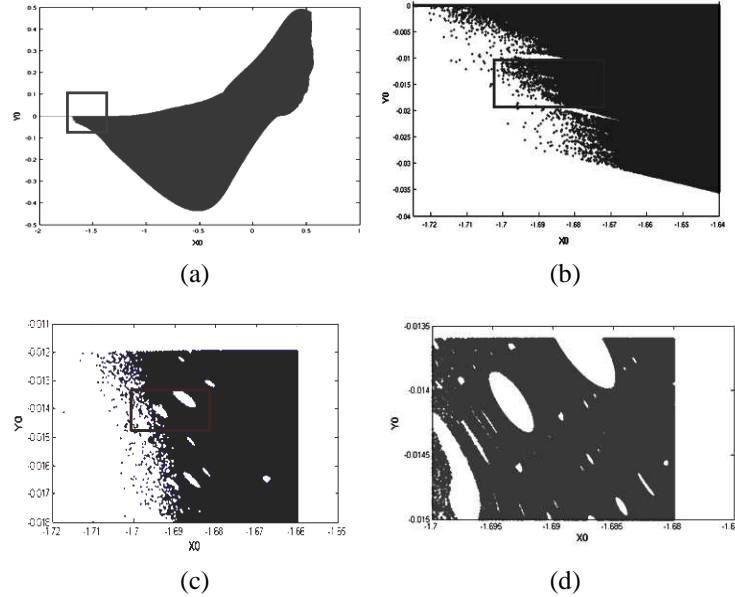

(a)   (b)

(c)   (d)

Fig. 6. The 2-D M-type fractal set of the map (21) and (22)
with a structure of Hole in the set.

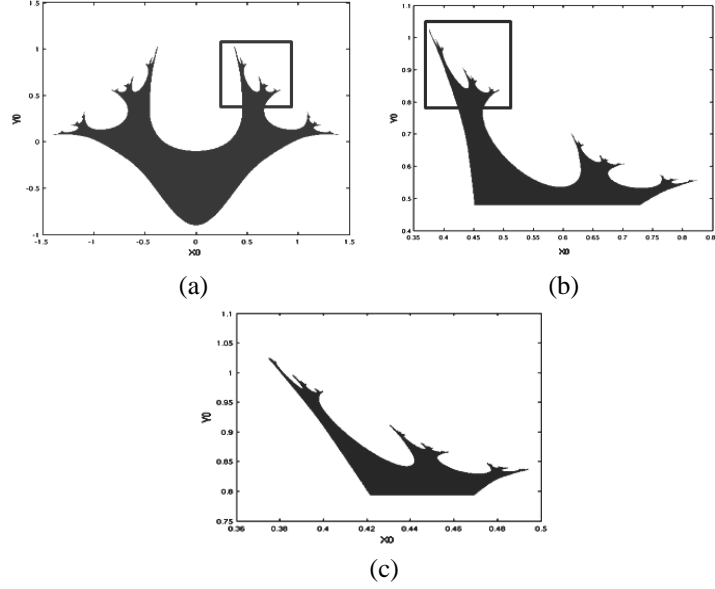(a)   (b)

(c)

Fig. 7. The 2-D J-type fractal set of the map (21) and (22)
($k_1=k_2=-0.5$) with a shaped structure of Horn.

and three real constants $\{b_1, b_2, b_3\}$ as

$$x_{n+1} = a_1 g_1(x_n, y_n, z_n) + b_1, \tag{27}$$

$$y_{n+1} = a_2 g_2(x_n, y_n, z_n) + b_2, \tag{28}$$

$$z_{n+1} = a_3 g_3(x_n, y_n, z_n) + b_3, \tag{29}$$

here it should be noticed that solutions $\{x_n, y_n, z_n\}$ to (27)-(29) are chaotic, but have
no exact chaos solutions (24)-(26).
For example, from the case of three chaos solutions;

$$x_n = \cos(C 2^n), \tag{30}$$

$$y_n = \sin(C 2^n), \tag{31}$$

$$z_n = \sin^2(C 2^n), \tag{32}$$

to the kernel map $x_{n+1} = x_n^2 - y_n^2 = x_n^2 - z_n$, $y_{n+1} = 2x_n y_n$ and $z_{n+1} = 4x_n^2 y_n^2 = 4x_n^2 z_n$, we
derive the following 3-D chaos map;

$$x_{n+1} = a_1(x_n^2 - z_n) + b_1, \tag{33}$$

344

$$y_{n+1} = a_2 x_n y_n + b_2, \tag{34}$$

$$z_{n+1} = a_3 x_n^2 z_n + b_3, \tag{35}$$

where the case of $(b_1, b_2, b_3) = (x_0, y_0, z_0)$ or (k_1, k_2, k_3) is a 3-D M-type or J-type chaos map, respectively. The fractal sets are defined by

$$M_3 = \{x_0, y_0, z_0 \in \mathbf{R} \ \left| \lim_{n \to \infty} x_n, y_n, z_n < \infty \right. \}, \tag{36}$$

and are illustrated in Figures 8 and 9 for the M-type and the J-type fractal sets with initial values $\{x_0, y_0, z_0\}$ and real constants $\{k_1, k_2, k_3\}$. The fractal structure in the set of Figures 8(a) and (b) has 3-D Holes corresponding to Figure 6(c) [12]. The shape has a physical analogue, for example, of Banana (Figure 8(c)), and the Holes close to the skin (Figure 8(d)) correspond qualitatively to the 2-D Holes of Figure 6(c). In Figure 9, the shape of the set has a fractal structure of 3-D Horn (Figures 9(a) and (b)) on the surface of the set, which has a physical analogue of the Horn of Deer (Figure 9(c)) corresponding to the 2-D fractal set (Figure 7(a)).
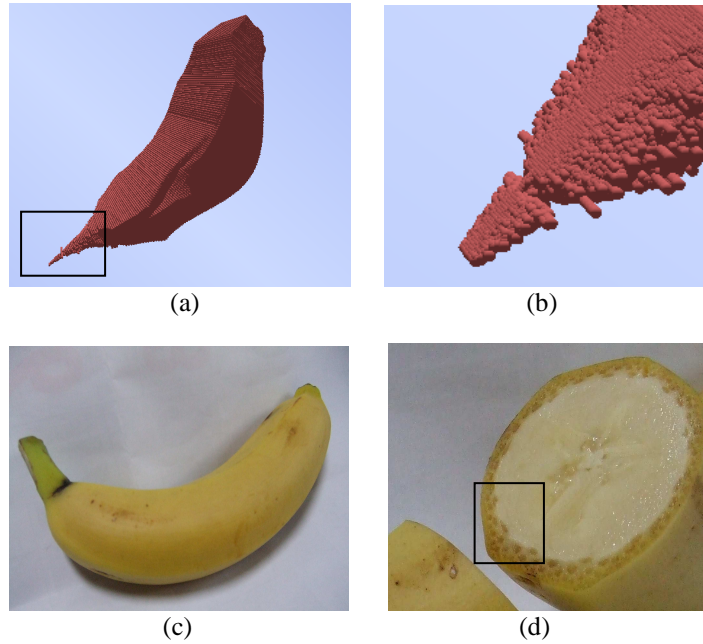

(a)　　　　　　　　　　(b)

(c)　　　　　　　　　　(d)

Fig. 8. A 3-D M-type fractal set in the $x_0 - y_0 - z_0$ space for (a_1, a_2, a_3) = (1.0, 2.0, 4.0) in (33) - (35), and the physical analogue (c) and (d).
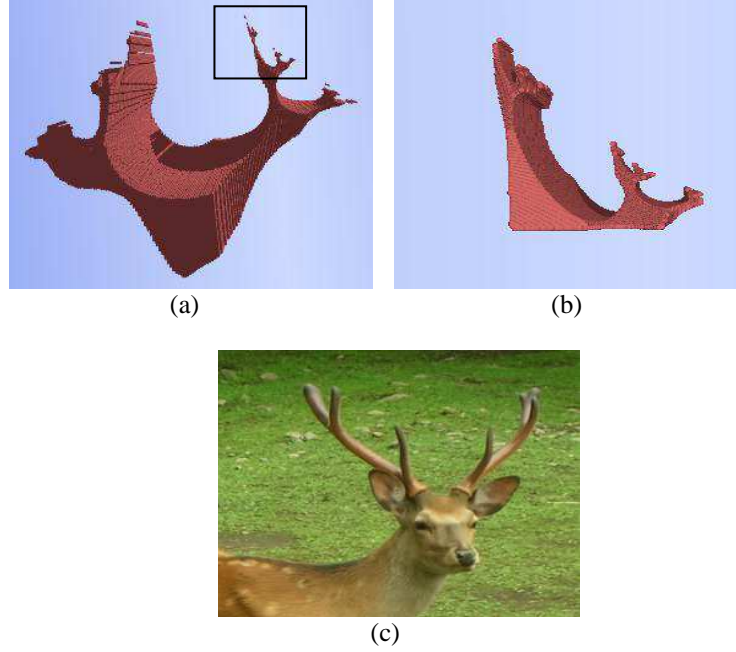
Fig. 9. A 3-D J-type fractal set in the $x_0 - y_0 - z_0$ space for $(a_1, a_2, a_3) = (1.0, 2.0, 4.0)$ and $(k_1, k_2, k_3) = (-0.5, 1.6, -0.5)$ in (33) - (35), and the physical analogue (c).

In this paper, we introduce an iteration number 300 to get each element of the set, the convergence condition $x_n^2 + y_n^2 < 4.0$, and the numerical calculation software MATLAB and POV-Ray for fractal sets $\{M_1, M_2, M_3\}$.

Conclusions

We have derived firstly the 1-D GLM with the physical analogue of population growth, and have considered the bifurcation diagrams, the fractal sets, the chaotic time series and the structure of the 1-D GLM based on an exact chaos solution. Then, the proposed approach is applied to the construction of the 2-D chaos maps without complex variables, which include the Mandelbrot map and the Julia map. Finally, we have expanded it to the construction of 3-D chaos maps based on three chaos solutions, and to the calculation of fractal set with physical analogue, defined in the x_0-y_0-z_0 space.

References

1. R. E. Amritkar and P. M. Gade. Wavelength doubling bifurcations in coupled map lattices. *Phys. Rev. Lett.* 70:3408－3411, 1993.
2. E. Barreto, B. R. Hunt, C. Grebogi and J. A. Yorke. From high dimensional chaos to stable periodic orbits: The structure of parameter space. *Phys. Rev. Lett.* 78:4561－4564, 1997.
3. Y. Gu, M. Tung, J. M. Yuan, D. H. Feng and L. M. Narducci. Crises and hysteresis in coupled logistic maps. *Phys. Rev. Lett.* 52:701－704, 1984.
4. O. B. Isaeva, S. P. Kuznetsov and V. I. Ponomarenko. Mandelbrot set in coupled logistic maps and in electronic experiment. *Phys. Rev.* E64, 055201, 2001.
5. L. P. Kadanoff. Where's the physics? *Phys. Today* 39:6－7, 1986.
6. S. Kawamoto and T. Horiuchi. Algorithm for exact long time chaotic series and its application to cryptosystems. *Int. J. Bifurcation and Chaos* 14:3607－3611, 2004.
7. B. B. Mandelbrot. *The Fractal Geometry of Nature.* Freeman, San Francisco, 1982.
8. R. M. May. Biological populations with non-overlapping generations: Stable points, stable cycles, and chaos. *Science* 15:645–646, 1974.
9. R. M. May. Simple mathematical models with very complicated dynamics. *Nature* 261:459－467, 1976.
10. P. Melby, J. Kaidel, N. Weber and A. Hubler. Adaptation to the edge of chaos in the self-adjusting logistic map. *Phys. Rev. Lett.* 84:5991－5993, 2000.
11. F. C. Moon. *Chaotic and Fractal Dynamics.* Wiley, New York, pp 346 －347, 1992.
12. N. T. Nhien, D. V. Liet and S. Kawamoto. Three-dimensional chaos maps and fractals. Abstracts Book of Dynamical Systems 100 years after Poincare. Gijon, Spain, pp 72 – 74, 2012.
13. S. Raghavachari and J. A. Glazier. Spatially coherent states in fractaly coupled map lattices. *Phys. Rev. Lett.* 74:3297－3300, 1995.
14. T. U. Singh, A. Nandi, R. Ramaswamy. Coexisting attractors in periodically modulated logistic maps. *Phys. Rev.* E77:066217, 2008.
15. J. Toyama and S. Kawamoto. Generation of pseudo-random numbers by chaos-type function and its application to cryptosystems. *Electrical Engineering in Japan* 163:67－74, 2008.

Stability of State-Period Dependent Non-linear Hybrid Dynamical System

Yutsuki Ogura[1], Hiroyuki Asahara[2] and Takuji Kousaka[1]

[1] Faculty of Engineering, Oita University, 700 Dannoharu, Oita, Japan
(E-mail: yutsuki@bifurcation.jp, takuji@oita-u.ac.jp)
[2] Faculty of Engineering, Fukuoka University, 19-1, Nanakuma 8, Jonan-ku, Fukuoka, Japan
(E-mail: asahara@bofurcation.jp)

Abstract. We propose a stability analysis method applicable to a simple non-linear hybrid dynamical system (HDS). First, we define the two-dimensional non-linear HDS and its behavior. Next, we use Taylor expansion around the period-one orbit to derive the perturbation between of the orbits, which is the finding of this study. Moreover, we consider the evolution of the perturbation and analyze the stability of the period-one orbit. Finally, we apply the proposed method to a non-linear interrupted circuit and confirm its validity.
Keywords: Hybrid dynamical system, Stability analysis, Bifurcation, Period-one orbit.

1 Introduction

Hybrid dynamical system (HDS) has interrupted characteristics depending on the state and a periodic interval. Impacting systems [1], neuron models [2] and power electronic circuits [3] are typical examples of HDS. In addition, we know that the bifurcation phenomena occur upon varying the parameter values. Researchers have reported that the bifurcation phenomenon changes the qualitative property [4]. Therefore, analyzing the bifurcation phenomena is important in order to solve engineering problems.

The bifurcation phenomena observed in the HDS are classified into two types. One depends on the characteristic multiplier of the Jacobian matrix, which is called the local bifurcation [5]. The period-doubling bifurcation, saddle-node bifurcation, neimark-sacker bifurcation are known as the examples of the local bifurcation. These bifurcation phenomena have studied in many papers. On the other hand, border-collision bifurcation, grazing bifurcation, corner-collision bifurcation are called the global bifurcation [6]. We can analyze them based on the normal form map, which uses the characteristic multiplier [7]. Therefore, deriving the characteristic multiplier is important for investigating the bifurcation phenomena.

Deriving the characteristic multiplier of the Jacobian matrix is called stability analysis. Poincaré map method and Filippov's method are the examples of the stability analysis method for HDS [8, 9]. Each method has advantages and disadvantages respectively. For example, we can apply Poincaré map method for both linear and non-linear HDS but the calculation process of the Jacobian matrix is complicated. So this method is unsuitable to analyze the stability of high-dimensional

HDS. On the other hand, Filippov's method is able to apply for linear HDS even if the HDS has high-dimensional topology. However, we can not apply this method to non-linear HDS.

In this paper, based on Filippov's theory, we propose a stability analysis method for non-linear hybrid dynamics system which depends on the state and periodic interval. First, we define the two-dimensional non-linear HDS. Next, we explain the method to derive stability of period-one orbit. Furthermore, we consider its state transition matrices (called the monodromy matrix) using Taylor expansion. Finally, we apply proposed method for a non-linear interrupted circuit and confirm its performance.

2   Analytical method

2.1   Two-dimensional non-linear hybrid dynamical system

We consider the two-dimensional non-linear dynamical dynamical system described by the following differential equations

$$\frac{d\boldsymbol{x}}{dt} = \boldsymbol{f}(\boldsymbol{x}, \boldsymbol{\lambda}) = \begin{cases} \boldsymbol{f}_1(\boldsymbol{x}, \boldsymbol{\lambda}_1), & \text{subsystem-1} \\ \boldsymbol{f}_2(\boldsymbol{x}, \boldsymbol{\lambda}_2), & \text{subsystem-2} \end{cases}, \tag{1}$$

where $t \in \boldsymbol{R}$, $\boldsymbol{x} \in \boldsymbol{R}^2$ and $\boldsymbol{f} : \boldsymbol{R}^2 \to \boldsymbol{R}^2$, and which has two subsystems. Now, Eq. (1) is written by the following equations

$$\boldsymbol{x}(t - kT) = \boldsymbol{\varphi}(t - kT, \boldsymbol{x}_k, \boldsymbol{\lambda}) = \begin{cases} \boldsymbol{\varphi}_1(t - kT, \boldsymbol{x}_k, \boldsymbol{\lambda}_1), & \text{subsystem}{-}1 \\ \boldsymbol{\varphi}_2(t - kT, \boldsymbol{x}_k, \boldsymbol{\lambda}_2), & \text{subsystem}{-}2 \end{cases}, \tag{2}$$

when $\boldsymbol{x}_k$ means the solution at arbitrary time $t = kT$ as $t \geq kT$. In adding, we define the switching section $\varSigma$ composed of scalar function $q : \boldsymbol{R}^2 \to \boldsymbol{R}^2$ as follows

$$\varSigma = \{\boldsymbol{x} \in \boldsymbol{R}^2 : q(\boldsymbol{x}) = 0, q : \boldsymbol{R}^2 \to \boldsymbol{R}\}, \quad q(t + T, x) = q(t, x). \tag{3}$$

Next, we explain the behavior of the orbit observed in this system. When the solution reaches to $\varSigma$, subsystem-1 changes to subsystem-2. If the periodic forces add to subsystem-2, it changes to subsystem-1. However, this switching event does not occur when the periodic forces add to subsystem-2. The behavior observed in periodic interval T can be classified roughly into two cases. Case(a) is that the orbit keep subsystem-1 in periodic interval T. On the other hand, in case(b), the switching event occurs. In case(a), the solution at $t = (k + 1)T$ is written as follows

$$\boldsymbol{x}_{k+1} = F(\boldsymbol{x}_k) = \boldsymbol{\varphi}_1(T, \boldsymbol{x}_k, \boldsymbol{\lambda}_1). \tag{4}$$

In case(b), the solution at $t = (k + 1)T$ is written as follows

$$\boldsymbol{x}_{k+1} = F(\boldsymbol{x}_k) = P_2(P_1(\boldsymbol{x}_k)). \tag{5}$$

P_1 and P_2 in Eq. (5) are expressed by the following equations

$$P_1(\boldsymbol{x}_k) = \boldsymbol{\varphi}_1(t_\mathrm{a}, \boldsymbol{x}_k, \boldsymbol{\lambda}_1), \tag{6}$$

$$P_2(\boldsymbol{x}_k) = \boldsymbol{\varphi}_2(T - t_\mathrm{a}, P_1(\boldsymbol{x}_k), \boldsymbol{\lambda}_2), \tag{7}$$

where the interval which the system keeps subsystem-1 is t_a. From Eqs. (4) and (5), we can define period-one orbit observed in this system as follows

$$F^1(\boldsymbol{x}_k) - \boldsymbol{x}_k = 0. \tag{8}$$

And we describe the period-one orbit which satisfies Eq. (8) as follows

$$\boldsymbol{x}_{k+1}^* = \boldsymbol{\varphi}_j(T, \boldsymbol{x}_k^*, \boldsymbol{\lambda}_j), \quad j = 1 \text{ or } 2, \tag{9}$$

where $\boldsymbol{x}_k^*$ is the initial value at $t = kT$.

2.2 Stability of period-one orbit

Based on Floquet theory [10], we explain stability of period-one orbit. We consider the perturbations between the period-one orbit and the nearby one. The initial condition of nearby orbit is perturbed. The perturbations of both orbits at $t = 0$ and $t = T$ are decided as follows

$$\begin{aligned} \Delta\boldsymbol{x}_0 &= \boldsymbol{x}_0 - \boldsymbol{x}_0^*, \\ \Delta\boldsymbol{x}_1 &= \boldsymbol{x}_1 - \boldsymbol{x}_1^*. \end{aligned} \tag{10}$$

Relationship between $\Delta\boldsymbol{x}_0$ and $\Delta\boldsymbol{x}_1$ is expressed as

$$\Delta\boldsymbol{x}_1 = \boldsymbol{M}\Delta\boldsymbol{x}_0. \tag{11}$$

Now, we name $\boldsymbol{M}$ the monodromy matrix. Deriving the characteristic multipliers μ in Eq. (12) of the monodromy matrix $\boldsymbol{M}$, we can analyze stability of period-1 orbit

$$|\boldsymbol{M} - \mu \boldsymbol{I}_n| = \boldsymbol{0}. \tag{12}$$

The period-one orbit is stable if the characteristic multipliers satisfies $|\mu| < 1$.

First, we derive the monodromy matrix in case(a). Figure 1 shows the period-one orbit (gray line) and nearby one (black line) in case(a). From Eq. (2), $\boldsymbol{x}_1$ is described as

$$\boldsymbol{x}_1 = \boldsymbol{\varphi}_1(T, \boldsymbol{x}_0^* + \Delta\boldsymbol{x}_0, \boldsymbol{\lambda}_1). \tag{13}$$

Using Taylor expansion around $\boldsymbol{x}_0^*$, Eq. (13) is rewritten as follows

$$\boldsymbol{x}_1 = \boldsymbol{\varphi}_1(T, \boldsymbol{x}_0^*, \boldsymbol{\lambda}_1) + \frac{\partial \boldsymbol{\varphi}_1(T, \boldsymbol{x}_0^*, \boldsymbol{\lambda}_1)}{\partial \boldsymbol{x}_0^*} \Delta\boldsymbol{x}_0. \tag{14}$$

Therefore, the mondromy matrix $\boldsymbol{M}$ in case(a) is expressed as

$$\boldsymbol{M} = \frac{\Delta\boldsymbol{x}_1}{\Delta\boldsymbol{x}_0} = \frac{\partial \boldsymbol{\varphi}_1(T, \boldsymbol{x}_0^*, \boldsymbol{\lambda}_1)}{\partial \boldsymbol{x}_0^*}. \tag{15}$$
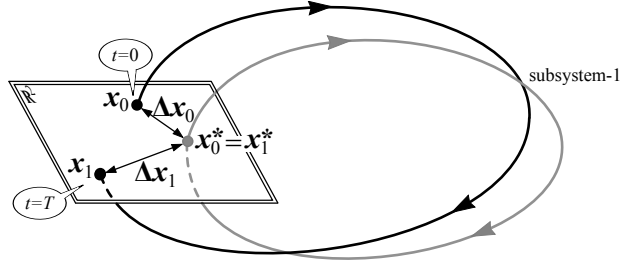
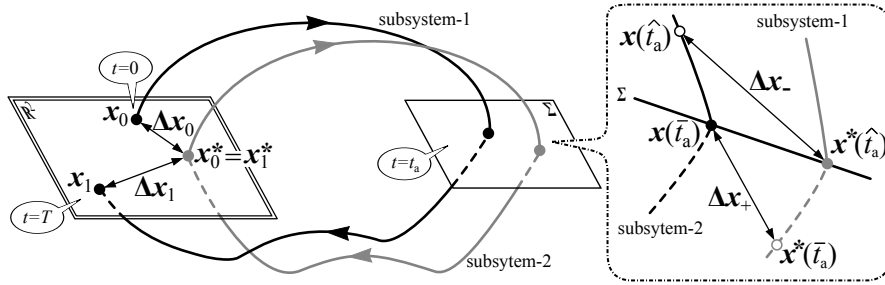**Fig. 1.** A conceptual diagram of the monodromy matix without switching

Fig. 2. A conceptual diagram of the monodromy matix with switching

Next, we derive the monodromy matrix in case(b). Figure 2 shows the two orbits and the enlarged view around the switching section Σ. In the enlarged view, $\hat{t}_\mathrm{a}$ is the interval which the period-one orbit keeps subsystem-1. On the other hand, the nearby one keeps subsystem-1 for $\bar{t}_\mathrm{a}$. From Eq. (2), $x(\hat{t}_\mathrm{a})$ and x_1 and described respectively as

$$x(\hat{t}_\mathrm{a}) = \varphi_1(\hat{t}_\mathrm{a}, x_0^* + \Delta x_0, \lambda_1), \tag{16}$$

$$x_1 = \varphi_2(T - \bar{t}_\mathrm{a}, x^*(\bar{t}_\mathrm{a}) + \Delta x_+, \lambda_2). \tag{17}$$

Using Taylor expansion around x_0^*, Eq. (16) is rewritten as follows

$$x(\hat{t}_\mathrm{a}) = \varphi_1(\hat{t}_\mathrm{a}, x_0^*, \lambda_1) + \frac{\partial \varphi_1(\hat{t}_\mathrm{a}, x_0^*, \lambda_1)}{\partial x_0^*} \Delta x_0. \tag{18}$$

Similarly, using Taylor expansion around $x^*(\bar{t}_\mathrm{a})$, Eq. (17) is rewritten by the following equation

$$x_1 = \varphi_2(T - \bar{t}_\mathrm{a}, x^*(\bar{t}_\mathrm{a}), \lambda_2) + \frac{\partial \varphi_2(T - \bar{t}_\mathrm{a}, x^*(\bar{t}_\mathrm{a}), \lambda_2)}{\partial x^*(\bar{t}_\mathrm{a})} \Delta x_+. \tag{19}$$

From the above, the monodromy matrix M in case(b) is expressed as

$$M = \frac{\partial(\varphi_2(T - \bar{t}_\mathrm{a}, x^*(\bar{t}_\mathrm{a}), \lambda_2))}{\partial x^*(\bar{t}_\mathrm{a})} S \frac{\partial(\varphi_1(\hat{t}_\mathrm{a}, x_0^*, \lambda_1))}{\partial x_0^*}. \tag{20}$$

Here, matrix S is called the saltation matrix and described as follows

$$S = I_n + \frac{(f_2 - f_1)n^\top}{n^\top f_1 + \left.\dfrac{\partial q(x(t))}{\partial t}\right|_{t=t_a}},$$
(21)

where I_n is the identity matrix.

3 Example of the application

In this chapter, we apply proposed method to the two-dimensional interrupted circuit. The two-dimensional non-linear interrupted circuit is presented in Fig. 3. The circuit equations are given by

$$\begin{cases} L\dfrac{di}{dt} = -ri - v \\ C\dfrac{dv}{dt} = i - G(v) + \dfrac{E_1 - v}{R_0 + R_1} \end{cases}, \quad \text{for switch-1,}$$
(22)

$$\begin{cases} L\dfrac{di}{dt} = -ri - v \\ C\dfrac{dv}{dt} = i - G(v) + \dfrac{E_2 - v}{R_0 + R_2} \end{cases}, \quad \text{for switch-2,}$$
(23)

where $G(v)$ denotes non-linear resistor and is expressed as

$$G(v) = -a \tanh(bv).$$
(24)

Figure 4 shows behavior of the orbit observed in this system. We assume that the initial inductance current i_k and the initial capacitance voltage v_k at $t = kT$ and the switch is position 1. When v reaches the reference voltage v_{ref}, the switch is turned to 2. The switch keeps position 2 until the arrial of the next clock pulse. If we replace with

$$y = \frac{v}{a}\sqrt{\frac{C}{L}}, \quad x = \frac{i}{a}, \quad \tau = \frac{1}{\sqrt{LC}}, \quad r_1 = \frac{1}{a}\frac{1}{R_0 + R_1}, \quad r_2 = \frac{1}{a}\frac{1}{R_0 + R_2},$$

$$B_1 = r_1 E_1, \quad B_2 = r_2 E_2, \quad g_1 = \frac{r_1\gamma}{b}, \quad g_2 = \frac{r_2\gamma}{b}, \quad k = r\sqrt{\frac{C}{L}}, \quad \gamma = ab\sqrt{\frac{L}{C}}.$$
(25)

Eqs. (22) and (23) are transformed into the following differential equations

$$f_1 = \begin{cases} \dfrac{dx}{d\tau} = -kx - y \\ \dfrac{dy}{d\tau} = x - g_1 y + \tanh(\gamma y) + B_1 \end{cases}, \quad \text{for switch-1,}$$
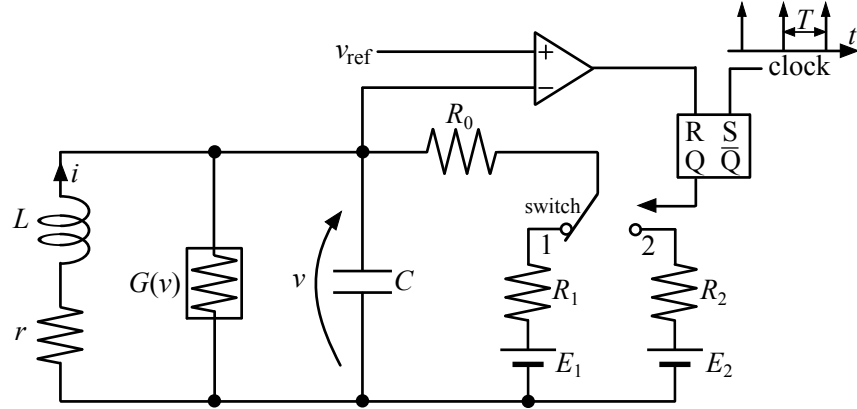(26)

Fig. 3. Two-dimensional non-linear interrupted circuit
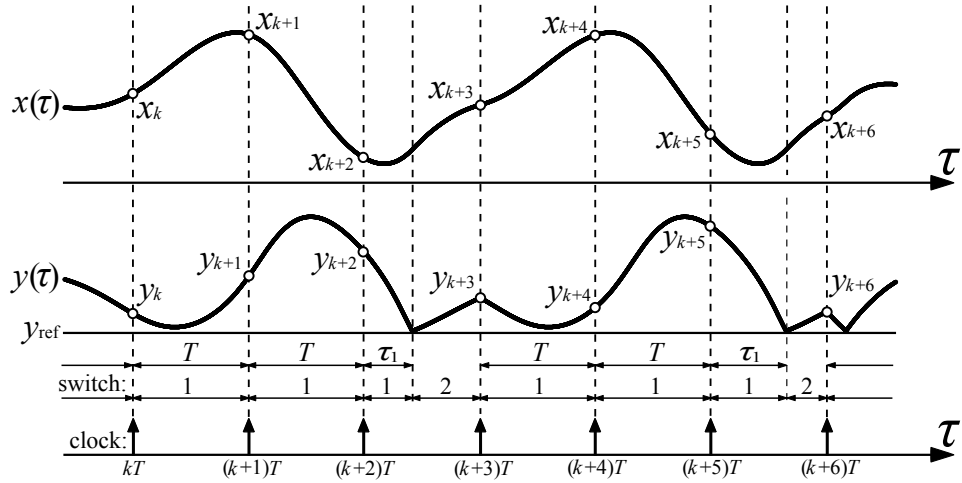

Fig. 4. Example of the orbit

$$f_2 = \begin{cases} \dfrac{dx}{d\tau} = -kx - y \\ \dfrac{dy}{d\tau} = x - g_2 y + \tanh(\gamma y) + B_2 \end{cases} , \quad \text{for switch-2,} \qquad (27)$$

We fix the following parameters shown in Eqs. (22) and (23)

$$k = 0.1, \quad \gamma = 1.6, \quad y_{\text{ref}} = -0.67,$$
$$B_1 = 0.8, \quad B_2 = 1.3, \quad g_1 = 0.7, \quad g_2 = 2.5. \qquad (28)$$

Figure 5 shows the 1-parameter bifurcation diagram upon varying the bifurcation parameter T. From Fig. 5 we observe that the bifurcation phenomenon for

period-1 solution occur around $T = 11.1$. Here, we consider (a) and (b) in Fig. 5. Figure 6 shows the phase planes at (a) and (b). Therefore, we presume that the bifurcation phenomenon around $T = 11.1$ is period-doubling bifurcation. Table 1 shows the application result of the proposal method. In table 1, μ_1 and μ_2 are the characteristic multipliers of the monodromy matrix corresponding to the bifurcation parameter T. Table 1 indicates that period-doubling bifurcation occurs at $T = 11.10961$. From this result, we confirmed the validity of our proposed method.

4   Conclusion

In this paper, we have proposed a stability analysis method applicable to a simple non-linear HDS. First, we defined the two-dimensional non-linear HDS and its behavior. Next, we used Taylor expansion around the period-one orbit to derive the perturbation between the orbit and nearby one. Moreover, we considered the evolution of the perturbation and analyze stability of the period-one orbit. Finally, we applied this method for a non-linear interrupted circuit, and we confirm the validity of this method.

References

1. S. F. Masri, "Analitical and experimental studies of multiple-unit impact dampers," *Journal of the Acoustical Society of America*, Vol. 45, pp. 1111-1117,1969.
2. E. M. Izhikevich, "Simple model of spiking neurons," *IEEE Transactions of Neural Networks*, Vol. 14, No. 6, pp. 1569-1572, 2003.
3. Kawakami H, Lozi R, "Switched dynamical systems — dynamical of a class of circuits with switch," *Proceedings of the RIMS Conference on Structure and Bifurcations of Dynamical Systems*, World Scientific: Singapore, 1992; 39-58.
4. S. Hayashi, "Periodically interrupted electric circuits," *Denki-Shoin*, 1961.
5. C. K. Tse, "Flip Bifurcation and Chaos in Three-state Boost Switching Regulators," IEEE Transaction on Circuits and Systems I, Vol.41, No. 1, pp. 16-23, 1994.
6. H. E. Nusse, J. A. Yorke, "Border-Collision Bifurcations including Period Two to Period Three for Piecewise Smooth Systems," Physica D, Vol. 57, pp. 39-57, 1992.
7. S. Banerjee, C. Grebogi, "Border Collision Bifurcations in Two-Dimensional Piecewise Smooth Maps," Physical Review E, Vol. 59, No. 4, pp. 4052-4061, 1999.
8. G. Ikeda, A. Kazuyuki, T. Kousaka, "Calculation Method of Bifurcation Point for an Impact Oscillator with Periodic Function," *Proc. CHAOS 2012.*
9. R. I. Leine, D. H. V. Campen, B. L. V. de Vrande, "Bifurcations in nonlinear discontinuous systems," *Nonlinear Dynamics*, Vol. 23, pp. 105-164, 2000.
10. G. Floquet, "Sur les équations differentielles linéaires á coefficients périodiques," *Ann. Sci. Ecole Norm. Sup.*, Ser. 2. 12, p. 47, 1883.
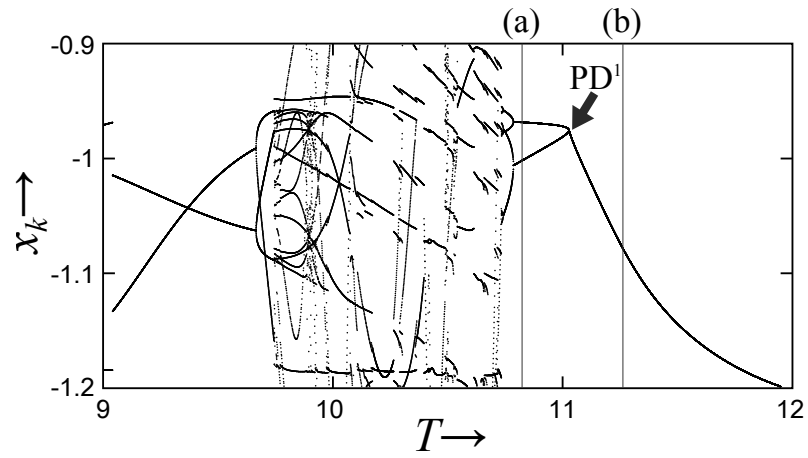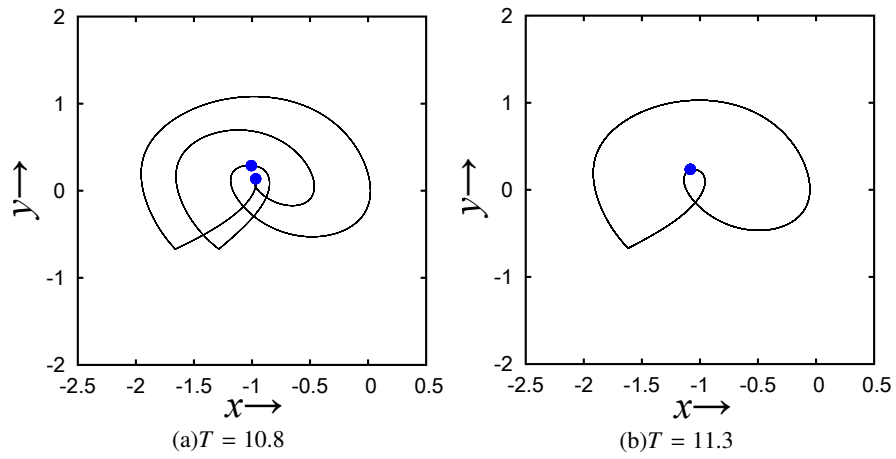
Fig. 5. One-parameter bifurcation diagram

(a)$T = 10.8$ (b)$T = 11.3$

Fig. 6. The phase planes

Table 1. Application result

T	μ_1	μ_2	Remarks
11.12000	-0.10616	-0.87017	Stable
11.11000	-0.10050	-0.99499	Stable
$\vdots$	$\vdots$	$\vdots$	$\vdots$
11.10961	-0.10032	-1.00000	PD[1]
$\vdots$	$\vdots$	$\vdots$	$\vdots$
11.10000	-0.09612	-1.12860	Unstable
11.09000	-0.09266	-1.27292	Unstable

A vision of the Brownian motion models useful in random systems analysis

Gabriel V. Orman and Irinel Radomir

Department of Mathematics and Computer Science "Transilvania" University of Braşov, 500091 Braşov, Romania
(E-mail: `ogabriel@unitbv.ro`)

Abstract. There are many cases when we refer to *chaos* and *chaotic and complex systems* to describe the comportment of some natural phenomena. In this context, we shall discuss, in this paper, some aspects which appear in the study of various systems. Firstly, we shall refer to the *Brownian transition probabilities* in connection with the conditions assumed on the transition probabilities; and then the *standard Brownian motion* is considered in connection with the "passage times" which are the most important Markov times.

Keywords: stochastic differential equations, stochastic calculus, Markov processes, Markov property, Brownian motion.

1 Introduction

Starting from the observation that many a time we refer to *chaos* and *chaotic and complex systems* to describe the comportment of some natural phenomena, it is very useful, from a mathematical point of view, to talk about a passing *from chaotic and complex systems to Brownian motion*. In this way we can refer to the *Brownian motion* which is a more realistic model of such phenomena.

Its fascinating properties and its far-reaching extension of the simplest normal limit theorems to functional limit distributions acted, and continue to act, as a catalyst in random systems analysis. As some authors remarks too, the Brownian motion reflects a perfection that seems closer to a law of nature than to a human invention.

In Physics, the ceaseless and extremely erratic dance of microscopic particles suspended in a liquid or gas, is called *Brownian motion*. It was systematically investigated by Robert Brown (1828, 1829), an English botanist, from movement of grains of pollen in water to a drop of water in oil. He was not the first to mention this phenomenon and had many predecessors but Brown's investigation brought it to the attention of the scientific community.

Brownian motion was frequently explained as due to the fact that particles were alive. It is only in 1905 that kinetic molecular theory led Einstein to the first mathematical model of Brownian motion. He began by deriving its possible existence and then only learned that it had been observed.

A completely different origin of mathematical Brownian motion is a game theoretic model for fluctuations of stock prices due to L. Bachélier from 1900. In his doctoral thesis, *Théorie de la spéculation*, Ann. Sci. École Norm. Sup., 17, 1900, 21-86, he hinted that it could apply to physical Brownian motion. Therein, and in his subsequent works, he used the heat equation and, proceeding by analogy with *heat propagation* he found, albeit formally, distributions of various functionals of mathematical Brownian motion. Heat equations and related parabolic type equations were used rigorously by Kolmogorov, Petrovsky, Khintchine.

But Bachélier was unable to obtain a clear picture of the Brownian motion and his ideas were unappreciated at the time. This because a precise definition of the Brownian motion involves a measure on the path space, and it was not until 1908-1909 when É. Borel published his classical memoir on Bernoulli trials: *Les probabilités dénombrables et leurs applications arithmétique*, Rend. Circ. Math. Palermo 27, 247-271, 1909. But as soon as the ideas of Borel, Lebesgue and Daniell appeared, it was possible to put the Brownian motion on a firm mathematical foundation. And this was achived in 1923 by N. Wiener, in his work: *Differential space*, J. Math. Phys. 2, 131-174, 1923.

Many researchers were fascinated by the great beauty of the theory of Brownian motion and many results have been obtained in the last decades. As for example, among other things, in *Diffusion processes and their sample paths* by K. Itô and H.P. McKean, Jr., in *Theory and applications of stochastic differential equations* by Z. Schuss, or in *Stochastic approximation* by M.T. Wasan as in *Stochastic calculus and its applications to some problems in finance* by J.M. Steele.

In fact, the construction of the Brownian motion as a limit of a rescaled random walk can be generalized to a class of Markov chains. In this context, at the 4th CMSIM international Conference, we discussed some aspects relating to the approximation in the study of Markov processes and Brownian motion; also, we referred to the Markov property from a perspective of K. Itô.

Itô's integral and other details and related topics in stochastic calculus and applications in random systems analysis are developed among other by B. Øksendal and A. Sulem, J.M. Steele, P. Malliavin, P. Protter, D.W. Stroock.

2   In short about transition probabilities

In some previous papers we have dicussed on Markov processes in a vision of K. Itô and we have emphasized the aspects regarding to the Markov property. In this context a fundamental concept is that of *transition probabilities* which will be considered, in short, below.

Let S be a *state space* and consider a particle which moves in S. Also, suppose that the particle starting at x at the present moment will move into the set $A \subset S$ with probability $p_t(x, A)$ after t units of time, "irrespectively of its past motion", that is to say, this motion is considered to have a *Markovian character*.

The *transition probabilities* of this motion are $\{p_t(x, A)\}_{t,x,A}$ and is considered that the time parameter $t \in T = [0, +\infty)$.

The state space S is assumed to be a *compact Hausdorff space with a countable open base*, so that it is homeomorphic with a compact separable metric space by the Urysohn's metrization theorem. The σ-field generated by the open space (the topological σ-field on S) is denoted by $K(S)$. Therefore, a *Borel set* is a set in $K(S)$.

It will be assumed that the transition probabilities $\{p_t(x, A)\}_{t \in T, x \in S, A \in K(S)}$ satisfy the following conditions:

(1) for t and A fixed,

      a) the transition probabilities are Borel measurable in x;

      b) $p_t(x, A)$ is a probability measure in A;

(2) $p_0(x, A) = \delta_x(A)$ (i.e. the δ-measure concentrated at x);

(3) $p_t(x, \cdot) \overset{weak}{\Longrightarrow} p_t(x_0, \cdot)$ as $x \to x_0$ for any t fixed, that is

$$\lim_{x \to x_0} \int f(y) p_t(x, dy) = \int f(y) p_t(x_0, dy)$$

for all continuous functions f on S;

(4) $p_t(x, U(x)) \longrightarrow 1$ as $t \searrow 0$, for any neighborhood $U(x)$ of x;

(5) the Chapman-Kolmogorov equation holds:

$$p_{s+t}(x, A) = \int_S p_t(x, dy) p_s(y, A).$$

It is interesting to observe that, if we define,

$$p_t(x, dy) = \frac{1}{t\sqrt{2\pi}} e^{-\frac{(y-x)^2}{2t^2}} dy \quad \text{in } R$$

$$p_t(\infty, A) = \delta_\infty A.$$

then, the conditions $(1) - (5)$ above are satisfied for *Brownian transition probabilities*.

Let now consider $C = C(S)$ to be the space of all continuous functions (it is a separable Banach space with the supremum norm). Then, the *transition operators* can be defined in a similar manner.

Definition 2.1 *The operators p_t, defined by*

$$(p_t f)(x) = \int_S p_t(x, dy) f(y), \quad f \in C$$

are called "transition operators".

And the conditions for the transition probabilities can be adapted to the transition operators.

Now the Markov process can be defined as follows

Definition 2.2 *A Markov process is a system of stochastic processes*

$$\{X_t(\omega), t \in T, \omega \in (\Omega, K, P_a)\}_{a \in S},$$

that is for each $a \in S$, $\{X_t\}_{t \in S}$ is a stochastic process defined on the probability space (Ω, K, P_a).

The transition probabilities of a Markov process will be denoted by $\{p(t, a, B)\}$. Now let us denote by $\{H_t\}$ the transition semigroup and let R_α be the resolvent operator of $\{H_t\}$.

The next results shows that $p(t, a, B)$, H_t and R_α can be expressed in terms of the process as follows:

Theorem 2.1 *Let f be a function in $C(S)$. Then*

1. *$p(t, a, B) = P_a(X_t \in B)$.*

2. *For $E_a(\cdot) = \int_\Omega \cdot P_a(d\omega)$ one has $H_t f(a) = E_a(f(X_t))$.*

3. *$R_\alpha f(a) = E_a\left(\int_0^\infty e^{-\alpha t} f(X_t) dt\right)$.*

Proof. One can observe that *1.* and *2.* follow immediately.

To prove *3.*, we will use the following equality:

$$R_\alpha f(a) = \int_0^\infty e^{-\alpha t} H_t f(a) dt = \int_0^\infty e^{-\alpha t} E_a(f(H_t)) dt.$$

Since $f(X_t(\omega))$ is right continuous in t for ω fixed, and measurable in ω for t fixed, it is therefore measurable in the pair (t, ω). Thus, we can use Fubini's theorem and therefore we obtain

$$R_\alpha f(a) = E_a\left(\int_0^\infty e^{-\alpha t} f(X_t) dt\right),$$

which proves *3.*

3   From chaotic motion to Brownian motion

In our days the Brownian motion is of ever increasing importance not only in Probability theory but also in classical analysis and its applications.

Frequently, Brownian motion was explained as due to the fact that particles were alive. Today we know that this motion is due to the bombardament of the particles by the molecules of the medium. In a liquid, under normal conditions, the order of magnitude of the number of these impacts is of 1020 per second.

Let us imagine a chaotic motion of a particle of colloidal size immersed in a fluid. Such a chaotic motion of a particle is called, usually, *Brownian motion* and the particle which performs such a motion is referred to as a *Brownian particle*. Such a chaotic perpetual motion of a Brownian particle is the result of the collisions of particle with the molecules of the fluid in which there is.

But this particle is much bigger and also heavier than the molecules of the fluid which it collide, and then each collision has a negligible effect, while the superposition of many small interactions will produce an observable effect.

On the other hand, for a Brownian particle such molecular collisions appear in a very rapid succession, their number being enormous. For a so high frequency, evidently, the small changes in the particle's path, caused by each single impact, are too fine to be observable. For this reason the exact path of the particle can be described only by statistical methods.

Thus, the influence of the fluid on the motion of a Brownian particle can be described by the combination of two forces in the following way:

1. The considered particle is much larger than the particle of the fluid so that the cumulated effect of the interaction between the Brownian particle and the fluid may be taken as having a hydrodynamical character. Thus, the first of the forces acting on the Brownian particle may be considered to be the forces of *dynamical friction*. It is known that the frictional force exerted by the fluid on a small sphere immersed in it is determined from the Stockes's law: *the drag force per unit mass acting on a spherical particle of radius a is given by* $-\beta\mathbf{v}$*, with* $\beta = \dfrac{6\pi a\eta}{m}$, where m is the mass of the particle, η is the coefficient of dynamical viscosity of the fluid, and $\mathbf{v}$ is the velocity of particle.

2. The other force acting on the Brownian particle is caused by the individual collisions with the particles of the fluid in which there is. This force produces instantaneous changes in the acceleration of the particle. Furthermore, this force is *random both in direction and in magnitude*, and one can say that it is a *fluctuating force*. It will be denoted by $\mathbf{f(t)}$. For $\mathbf{f(t)}$ the following assumptions are made:

a) The function $\mathbf{f(t)}$ is statistically independent of $\mathbf{v}(t)$.

b) $\mathbf{f(t)}$ has variations much more frequent than the variations in $\mathbf{v}(t)$.

c) $\mathbf{f(t)}$ has the average equal to zero.

In these conditions, the Newton's equations of motion are given by the following stochastic differential equation

$$\frac{dbfv(t)}{dt} = -\beta\mathbf{v}(t) + \mathbf{f}(t) \tag{1}$$

which is called the *Langevin's equation.*

From the Langevin's equation, the statistical properties of the function $\mathbf{f(t)}$ can be obtained if its solution will be in correspondence with known physical laws. One can observe that the solution of (1) determines the *transition probability density* (in brief *the transition density*) $\rho(\mathbf{v}, t\mathbf{v}_0)$ of the random process $\mathbf{v}(t)$, which verifies the equation

$$P(\mathbf{v}(t) \in A) \,|\, \mathbf{v}(0) = \mathbf{v}_0) = \int_A \rho(\mathbf{v}, t, \mathbf{v}_0)d\mathbf{v}. \tag{2}$$

We do not insist on these aspects, our purpose has been to introduce the concept of transition density.

Now following K. Itô ([7], [5]) we shall refer shortly to the *k-dimensional Brownian motion* and emphasize some of its results.

But, firstly, we shall remind some aspects ragarding to the *3-dimensional Brownian motion* discussed at the 6th CMSIM international Conference.

It is not difficult to observe that a definition of a *Markov process* as in Definition 2.2 not correspond to many processes that are of a real interest. For this reason it is useful to obtain an extension of this notion (such an extended notion has been proposed by K. Itô).

Let E be a separable Banach space with real coefficients and norm $|| \cdot ||$ and let also $L(E, E)$ be the space of all bounded linear operators $E \longrightarrow E$. It can be observed that $L(E, E)$ is a linear space.

Definition 3.1 *The collection of stochastic processes*

$$X = \{X_t(\omega) \equiv \omega(t) \in S,\, t \in T,\, \omega \in (\Omega, K, P_a)\}_{a \in S}$$

is called a "Markov process" if the following conditions are satisfied:

1) *the "state space" S is a complete separable metric space and $K(S)$ is a topological σ-algebra on S;*

2) *the "time internal" $T = [0, \infty)$;*

3) *the "space of paths" Ω is the space of all right continuous functions $T \longrightarrow S$ and K is the σ-algebra $K[X_t : t \in T]$ on Ω;*

4) *the probability law of the path starting at a, $P_a(H)$, is a probability measure on (Ω, K) for every $a \in S$ which satisfy the following conditions:*

    4a) $P_a(H)$ is $K(S)$-measurable in a for every $H \in K$;

    4b) $P_a(X_0 = a) = 1$;

    4c) $P_a(X_{t_1} \in E_1, \cdots, X_{t_n} \in E_n) =$
$$\int \cdots \int_{a_i \in E_i} P_a(X_{t_1} \in da_1) P_{a_1}(X_{t_2 - t_1} \in da_2) \ldots$$
$$\ldots P_{a_{n-1}}(X_{t_n - t_{n-1}} \in da_n) \qquad for \quad 0 < t_1 < t_2 < \ldots < t_n.$$

According to Definition 3.1, X will be referred as a *Markov process in the generalized sense.*

Now let X be a Markov process in a generalized sense and let us denote by **B**(S) the space of all bounded real $K(S)$-measurable functions. Also let us consider a function $f \in \mathbf{B}(S)$.

It is supposed that

$$E_a\left(\int_0^\infty |f(X_t)| dt\right) \tag{3}$$

is bounded in a. Therefore

$$Uf(a) = E_a\left(\int_0^\infty f(X_t) dt\right) \tag{4}$$

is well-defined and is a bounded $K(S)$-measurable function of $a \in S$.

The Uf is called *the potential* of f with respect to X. Having in view that $Uf = \lim_{\alpha \downarrow 0} R_\alpha f$, it is reasonable to write R_0 instead of U. Based on this fact, $R_\alpha f$ will be called *the potential of order α* of f.

Remark 3.1 *It is useful to retain that $R_\alpha f \in \mathbf{B}(S)$ for $\alpha > 0$; and generally $f \in \mathbf{B}(S)$ while $R_0 f(= Uf) \in \mathbf{B}(S)$ under the condition (3).*

Now the name *potential* is justified by the following theorem on *the 3-dimensional Brownian motion*

Theorem 3.1 *Let X be the 3-dimensional Brownian motion. If $f \in \mathbf{B}(S)$ has compact support, then f satisfies (3) and*

$$Uf(a) = \frac{1}{2\pi} \int_{R^3} \frac{f(b) db}{|b - a|} = \frac{1}{2\pi} \times Newtonian\ potential\ of\ t. \tag{5}$$

Let us denote by D a bounded domain in $R^n, n \geq 1$.

Definition 3.2 *A function g is called "harmonic" in D if g is C^∞ in D and if $\Delta g = 0$ (where C^∞ is the class of functions differentiable infinitely many times.).*

Now let f be a continuous function defined on the boundary ∂D and let us denote by X a k-dimensional Brownian motion defined as follows

Definition 3.3 *The k-dimensional Brownian motion is defined on $S = R^k$ by the equality*

$$p_t(a, db) = (2\pi t)^{-\frac{k}{2}} e^{-\frac{|b-a|^2}{2t}} db = N_t(b - a)db,$$

where $|b - a|$ is the norm of $b - a$ in R^k.

Given a k-dimensional Brownian motion X, if there exists a solution g for the Dirichlet problem (D, f)[1], then

$$g(a) = E_a(f(X_\lambda)), \tag{6}$$

where $\lambda \equiv \lambda_D$ = exit time from D (that is to say $\lambda_D = inf\{t > 0 : X_t \notin D\}$, the hitting time of D^C).

In this context an interesting result is given in the following theorem

Theorem 3.2 *If D is a bounded domain and g is a solution of the Dirichlet problem (D, f), then*

$$g(a) = E_a(f(X_\lambda))$$

where $a \in D$ and $\lambda = \lambda_D$.

On the other hand, the Dirichlet problem (D, f) has a solution if ∂D is smooth as it is prooved in the following theorem

Theorem 3.3 *If ∂D is smooth, then*

$$g(a) = E_a(f(X_\lambda)),$$

where $\lambda = \lambda_D$ = exit time from D, is the solution of the Dirichlet problem (D, f).

Note 3.1 *The expression "∂D is smooth" means that ∂D has a unic tangent plane at each point x of ∂D and the outward unit normal of the tangent plane at x moves continously with x.*

Remark 3.2 *Many other details regarding to the topics just discussed, proofs and some related problems can be found in [7], [6], [1], [5], [23], [14], [21], [13], [19], [17].*

---

[1]The Diriclet problem D, f is to find a continuous function $g = g_{D,f}$ on the closure $\overline{D} \equiv D \cup \partial D$ such that g is harmonic in D and $g = f \circ g \, \partial D$.

Conclusion 3.1 *The Brownian motion can be represented as a random sum of integrals of orthogonal functions. Such a representation satisfies the theoretician's need to prove the existence of a process with the four defining properties of Brownian motion, but it also serves more concrete demands, one of the most important being the "chaotic and complex systems analysis".*

Especially, the series representation can be used to derive almost all of the most important analytical properties of Brownian motion.

It can also give a powerful numerical method for generating the Brownian motion paths that are required in computer simulation.

References

[1] A.T. Bharucha-Reid. Elements Of The Theory Of Markov Processes And Their Applications. Dover Publications, Inc., Mineola, New York, 1997.

[2] W. Feller. An Introduction to Probability Theory and its Applications, vol. I, II. John Wiley & Sons, Inc., New York, London, 1960.

[3] I.I. Gihman and A.V. Skorohod. Stochastic Differential Equations. Springer-Verlag, Berlin, 1972.

[4] B.V. Gnedenko. The Theory of Probability. Mir Publisher, Moscow, 1976.

[5] K. Itô. Selected Papers. Springer, 1987.

[6] K. Itô and H.P. McKean Jr. Diffusion Processes and their Sample Paths. Springer-Verlag, Berlin Heidelberg, 1996.

[7] K. Itô. Stochastic Processes. Eds. Ole E. Barndorff-Nielsen and Ken-iti Sato. Springer, 2004.

[8] H.J. Kushner and G.G Yin. Stochastic Approximation Algorithms and Applications. Springer-Verlag New York, Inc., 1997.

[9] M. Loève. Probability theory I. Springer-Verlag, New York, Heidelberg Berlin, 1977.

[10] M. Loève. Probability theory II. Springer-Verlag, New York, Heidelberg Berlin, 1978.

[11] P. Malliavin. Integration and Probability. Springer-Verlag New York, Inc., 1995.

[12] B. Øksendal. Stochastic Differential Equations: An Introduction with Applications. Sixth Edition. Springer-Verlag, 2003.

[13] B. Øksendal and A. Sulem. Applied Stochastic Control of Jump Diffusions. Springer, 2007.

[14] P. Olofsson and M. Andersson. Probability, Statistics and Stochastic Processes, 2nd Edition. John Wiley & Sons, Inc., Publication, 2012.

[15] G.V. Orman. Lectures on *Stochastic Approximation Methods and Related Topics.* Preprint. "Gerhard Mercator" University, Duisburg, Germany, 2001.

[16] G.V. Orman. Handbook of Limit Theorems and Stochastic Approximation. "Transilvania" University Press, Brasov, 2003.

[17] G.V. Orman. On Markov Processes: A Survey of the Transition Probabilities and Markov Property. In C. H. Skiadas and I. Dimotikalis, editors, *Chaotic Systems: Theory and Applications*, 224-232, 2010, World Scientific Publishing Co Pte Ltd.

[18] G.V. Orman. On a problem of approximation of Markov chains by a solution of a stochastic differential equation. In: C.H. Skiadas, I. Dimotikalis and C. Skiadas, editors, *Chaos Theory: Modeling, Simulation and Applications*, 30-40, 2011, World Scientific Publishing Co Pte Ltd.

[19] G.V. Orman. Aspects of convergence and approximation in random systems analysis. LAP Lambert Academic Publishing, 2012.

[20] P. Protter. Stochastic Integration and Differential Equations: a New Approach. Springer-Verlag, 1990.

[21] Z. Schuss. Theory and Application of Stochastic Differential Equations. John Wiley & Sons, New York, 1980.

[22] J.M. Steele. Stochastic calculus and financial applications. Springer-Verlag New York, Inc. 2001.

[23] D.W. Stroock. Markov Processes from K. Itô Perspective. Princeton Univ. Press, Princeton, 2003.

[24] M.T. Wasan. Stochastic Approximation. Cambridge University Press, 1969.

The Mechanisms of Chaotization in Switching Power Converters with Compensation Ramp

Dmitrijs Pikulins

Riga Technical University, Riga, Latvia
E-mail: dmitrijs.pikulins@rtu.lv

Abstract: Recently much attention has been paid to investigation of nonlinear dynamics of switching power converters, as this kind of dynamical systems, being inherently hybrid, is capable of exhibiting a wide variety of well known smooth as well as novel non-smooth phenomena. This research shows the diversity of complex interactions of smooth bifurcations and border collisions in one of the most typical power circuits – boost converter under current mode control – applying the method of complete bifurcation groups. The effects of realistic parameters and implementation of compensation signals on the robustness of chaotic modes of operation are investigated and explained in details.
Keywords: Bifurcations, Chaos, Non-smooth phenomena, Switching power converters.

1. Introduction

It is common knowledge for the majority of engineers working in the field of power electronics, that the only acceptable operating regime of switching power converters (SPC) is the period-1 (P1) mode, when all waveforms repeat at the same rate as driving clock element. So, all the efforts of practicing engineers are directed to insurance of stable operation of DC-DC converters, eliminating the possibilities of occurrence of any subharmonic oscillations. On the other hand, recent investigations have shown that the operation of SPC in subharmonic or even chaotic modes allows achieving higher performance characteristics of these devices. In example, paper [1] presents the novel control strategy, allowing simple digital implementation and excellent transient response. The idea of the control is based on the use of various combinations of two different control pulses that from the point of view of nonlinear dynamics could be treated as operation in a variety of subharmonic regimes. The other research [2] shows the applicability of inherently arising chaotic modes of operation of switching converters to the reduction of high levels of electromagnetic noise, generated by this kind of devices. Thus it has been demonstrated, that contrary to generally accepted opinion, the non-linear operating modes of switching converters could be efficiently utilized, providing new progressive control perspectives.

The methodology of implementation of the control ramp is widely used as the compensation tool for the irregularities of the current loop, ensuring stable P1 operation of SPC. In general, the introduction of this compensating signal shifts the border of the first period-doubling bifurcation, estranging the appearance of

subharmonic oscillations that are usually avoided. However, the same ramp also modifies the structure of the parameter space even after the period-doubling bifurcation, defining noticeable changes in the dynamics of the system. This research is dedicated to exploration of different mechanisms of chaotization and further aftereffects in the operation of SPC, defined by the implementation of mentioned compensation technique.

It has been demonstrated during several last decades, that the conventional models and methodologies used to predict the appearance of subharmonic oscillations in switching power converters are generally oversimplified and not capable of providing reliable data in many cases [3]-[6]. This fact determined the development of great number of scientific researches dedicated to possible improvements of already existing models and to the introduction of new promising approaches. Recently one innovative methodology – method of complete bifurcation groups (MCBG) [7]-[9] – has been applied to investigation of rare phenomena and chaos in SPC, allowing the detection and detailed analysis of previously unobserved operating regimes. MCBG is utilized within current research in order to provide the most complete analysis of the observed non-linear phenomena in the dynamics of SPC.

The structure of the paper is as follows. The second section presents the simplified discrete-time model of the boost SPC, introducing the compensating ramp in the current control loop. The results of the complete bifurcation analysis, including the construction of bifurcation map and various bifurcation diagrams, are presented and discussed in section 3. The concluding remarks and comments are given in the last section.

2. The Model of Boost Converter with Compensation Ramp

The SPC under study is widely used boost converter with peak current mode control, exhibiting unstable dynamics as the duty cycle exceeds 0.5 [3]. The main methodology of extending the region of stable P1 operation in this kind of devices is the introduction of compensation ramp signal, which is also included in the dynamical model.
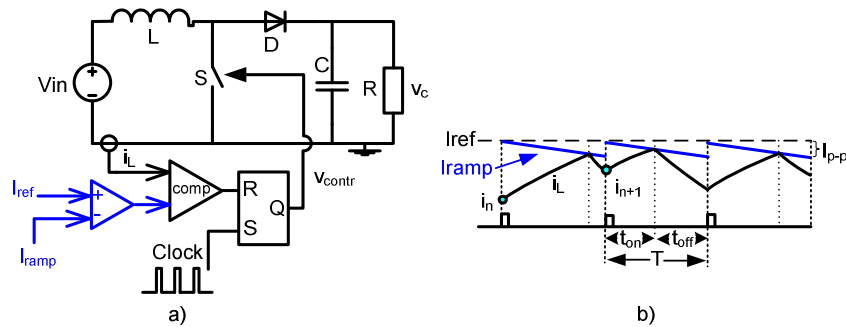

Fig. 1. (a) The simplified model of current - mode controlled boost converter; (b) waveforms of inductor current and compensation ramp.

The simplified model of boost SPC is shown in Fig. 1. The operation of converter is as follows: the switch is turned *ON* as the clock pulse arrives and turned *OFF* as the value of inductor current reaches the compensation ramp.

The dynamics of this energy conversion circuit could be described by two systems of difference equations, depending on the sequence of switching events. If the clock pulse arrives before the inductor current reaches the I_{ramp}, the obtained discrete time model is the following:

$$v_{n+1} = v_n e^{-T/(RC)}$$
$$i_{n+1} = i_n + V_{in} TL .$$

(1)

If the inductor current reaches I_{ramp} before the arrival of the next clock pulse the map would include the *ON* and *OFF* intervals:

$$v_{n+1} = e^{-mt_{off}} \left[K_1 \cos(\mu t_{off}) + K_2 \sin(\mu t_{off}) \right] + V_{in}$$
$$i_{n+1} = e^{-mt_{off}} \left[C[-m(K_1 \cos(\mu t_{off}) + K_2 \sin(\mu t_{off})) + \right.$$
$$\left. + \mu(-K_1 \sin(\mu t_{off}) + K_2 \cos(\mu t_{off}))] + (K_1 \cos(\mu t_{off}) \right.$$
$$\left. + K_2 \sin(\mu t_{off}))/R] + V_{in}/R,$$

(2)

where

$$t_{on} = (I_{ref} - i_n)/(V_{in}/L + S_c); \quad K_1 = v_n e^{-2mt_{on}} - V_{in};$$
$$t_{off} = T - t_{on}; \quad K_2 = \left[I_{ref}/C - \left(v_n e^{-2mt_{on}} + V_{in} \right) \right]/\mu;$$
$$m = 1/(2RC); \quad p = 1/\sqrt{LC}; \quad \mu = \sqrt{p^2 - m^2}; \quad S_c = I_{p-p}/T.$$

(3)

The borderline I_{border} defines the case, when the clock pulse arrives exactly at the time instance the inductor current reaches the control signal:

$$I_{border} = I_{ref} - T(V_{in}/L + S_c).$$

(4)

It has been shown that this discrete-time model could be efficiently applied to the study of nonlinear dynamics and estimation of stability boundaries of main period-1 and subharmonic modes of operation [8].

The provided model (1)-(4) is used in the process of the construction of bifurcation map, complete bifurcation diagrams, calculating parameters of different periodic regimes as well as estimating their stability.

The values of main parameters of boost converter under test are as follows: R=40 (Ω); L=1.5 (mH); C=5 (μF); T=100 (μS); V_{in}=5 (V); I_{ref}=[0.2…0.9] (A); S_c=[0…2000] (A/s).

3. Results of the complete bifurcation analysis

As it has been mentioned in the introduction, the analysis of the global dynamics of boost SPC will be provided by means of one of the most progressive techniques – method of complete bifurcation groups. This methodology has proved to be very useful during the complete analysis of nonlinear phenomena, observed in various classes of smooth as well as non-smooth dynamical systems [7]-[9].

The complete bifurcation analysis of the boost converter begins with the construction of bifurcation map, selecting reference current and compensation ramp as primary and secondary bifurcation parameters (see Fig. 2). As the mechanisms of chaotization are of special interest and the P1 orbits are not involved in the rapid transitions to chaotic modes of operation, the range of parameters defining stable P1 regime is disregarded in the constructed bifurcation map. As it could be seen from Fig. 2 for S_c=0 the classical period doubling route to chaos should be observed. As the value of compensation ramp is increased other subharmonic operation regimes (as well as periodic windows) just after the P2 appear, defining the formation and structure of chaotic regions.
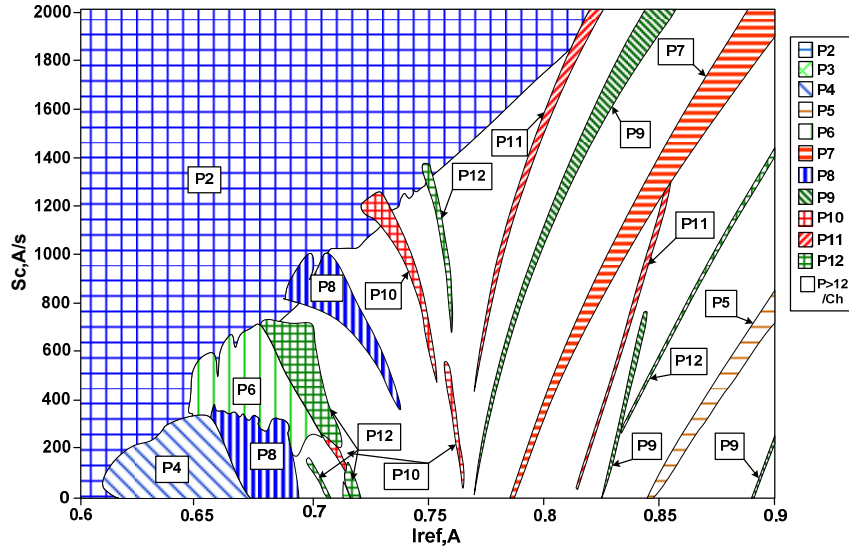
Fig.2. The bifurcation map of the boost converter.

This map will be referred to during the analysis of complete bifurcation diagrams, constructed as the horizontal cross-sections of Fig. 2.

It should be understood, that in this case the complete bifurcation diagrams are 3-dimensional graphs, depicting the sampled inductor current and capacitor voltage on two axes and the bifurcation parameter on the third one. For the clearness of analysis only the projection of this graph to the plane defined by the inductor current and the bifurcation parameter (I_{ref}) will be observed, as only in

this plane the collisions with the border defined by (4) could be precisely detected and interpreted.

In order to analyze the influence of the incrementing compensation ramp on the chaotization of the system, first let's examine the complete bifurcation diagram for the boost converter without the compensation.
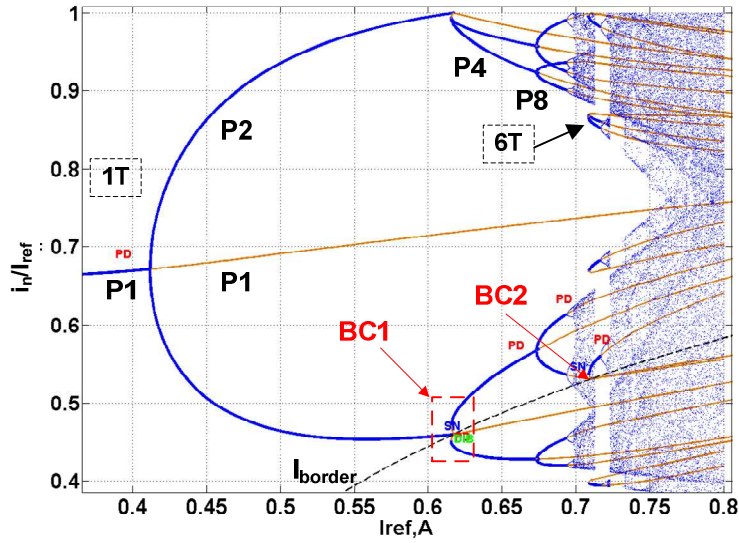

Fig. 3. The complete bifurcation diagram for S_c=0 (A/s).

The bifurcation diagram, depicting stable (dark lines) and unstable (light-colored lines) periodic regimes, as well as chaotic regions (shaded area), is shown in the Fig. 3. It could be seen, that for small values of reference current, the system operates in the stable P1 regime and moves to P2 mode through classical period doubling bifurcation. Further increment of I_{ref} leads to the development of non-smooth phenomena, when stable or unstable orbits collide with the I_{border} (dashed line), leading to non-smooth transition from P2 to P4 regimes (see point BC1), as well as change of shape of unstable branch of 6T bifurcation group (see point BC2). Thus it could be concluded, that for the selected set of system parameters, collisions with the border have slightly changed the topology of bifurcation diagram, without any noticeable rapid jumps between different modes of operation.

The second bifurcation diagram, constructed for S_c=200 (A/s) is shown in the Fig. 4. One of the most interesting features of the observed diagram is the presence of rather uncommon phenomena that will be referred as "cutting border collision" (CBC). It is well known, that the collision with borders in hybrid systems could lead to the appearance of non-smooth bifurcations, when the multipliers do not smoothly cross the unit circle, indicating the widely observed period-doubling or saddle-node bifurcations, but rather "jump" over

the border of unit circle, depicting the rapid change in the stability of definite regime under investigation. In the mentioned case the periodic regime still continues to exist, but its stability suddenly changes. However the CBC leads to the "disappearance" of all stable as well as unstable periodic regimes that cross the defined borderline.
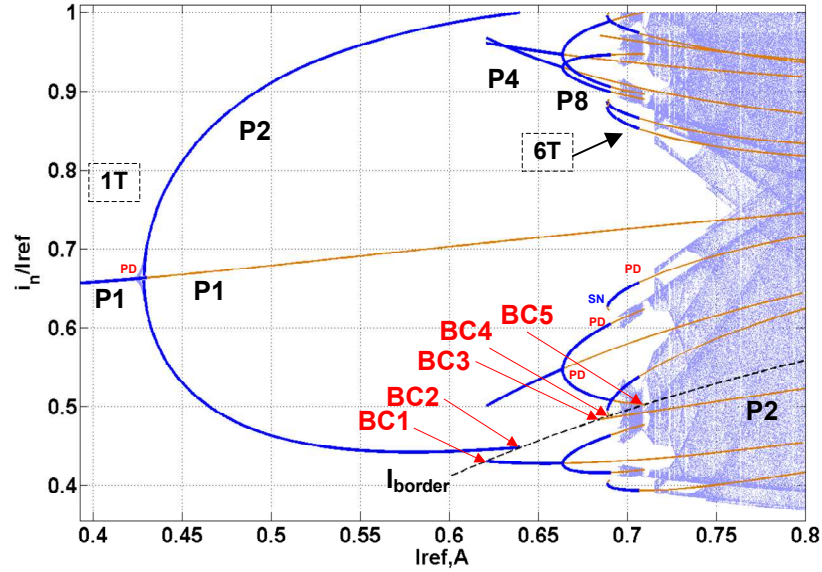

Fig. 4. The complete bifurcation diagram for S_c=200 (A/s).

This phenomenon could be observed, in example, in points BC1, BC2 and BC4 in the Fig. 4, where stable P2, P4 and unstable P8 regimes collide with the borderline defined in (4) and disappear without any signs of bifurcations. The route to chaos in this case is formed by rather uncommon period-doublings, leading to the infinite number of unstable periodic orbits and chaotic mode of operation.

It has been shown in the Fig. 3, that for S_c=0 (A/s) the border collision of 6T bifurcation group leads to some changes in the shape of bifurcation diagram. However the diagram in the Fig. 4 demonstrates that the same collision for S_c=200 (A/s) causes the disappearance of unstable branch of 6T bifurcation group, preserving the stable branch, leading to the development of independent chaotic regime.

It is interesting to note that the P2 orbit appears at point BC3 as unstable regime and continues to exist for larger values of I_{ref}. So it could be assumed that in the interval I_{ref}=[0.64…0.68] (A) this regime slides along the borderline (4). Other orbits after the CBC are not observed within the parameter range of interest.

As the transition from P2 to P4 in the Fig.4 is caused by highly non-smooth event, it would be interesting to investigate the topology of basins of attraction of coexisting P2 and P4 modes of operation for I_{ref}=0.63 (A).
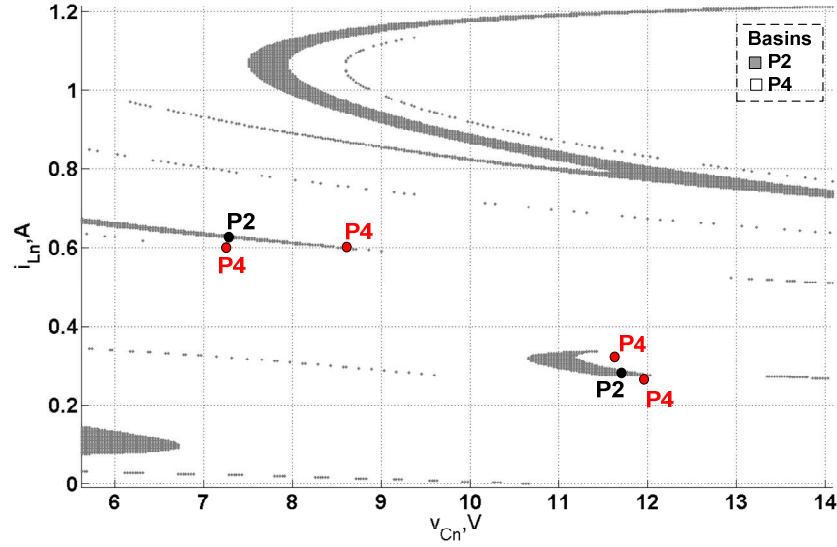
Fig. 5. Basins of attraction of P2 and P4 regimes for S_c= 200 (A/s) and I_{ref}=0.63 (A) with corresponding attractors.

As it could be seen from Fig. 5, despite the border collisions observed in the complete bifurcation diagrams, the basins of attraction of P2 and P4 regimes, forming rather complex structure, still remain smooth and no sign of uncommon topological peculiarities are observed.
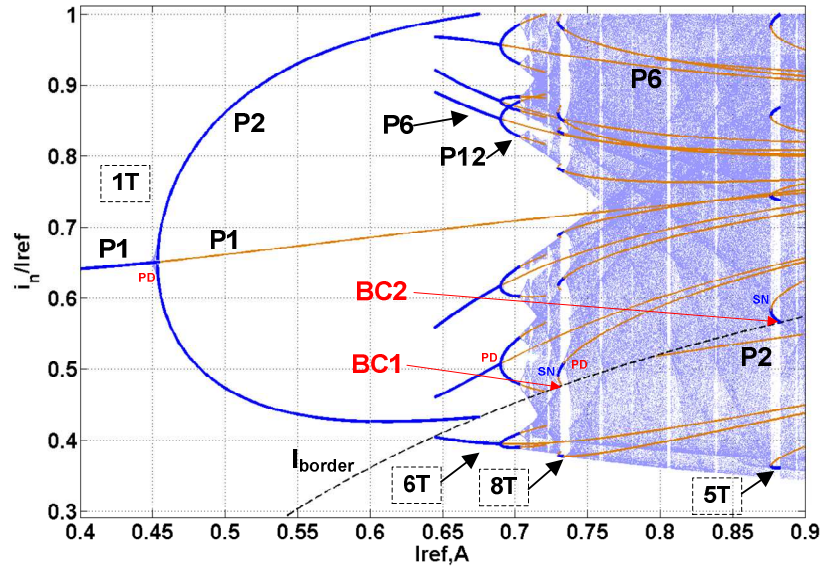

Fig. 6. The complete bifurcation diagram for S_c=500 (A/s).

Further increment of the compensation ramp practically leads to the enlargement of stable P1 region and essentially changes the sequence and types of bifurcations. Fig. 6 depicts the complete bifurcation diagram of the boost converter for S_c=500, showing that the first period doubling at I_{ref}=0.45 is followed by rapid transition from P2 to P6 operating regime with definite region of coexistence of both mentioned orbits. Further chaotization is governed by unstable orbits arising from the P6 regime through classical period-doublings.

Points BC1 and BC2 in the Fig. 6 demonstrate to possible interactions of periodic orbits, appearing from saddle-node bifurcations with the borderline (4). At point BC1 the cutting border collision eliminates only the unstable regime of 8T bifurcation group, allowing the gradual development of chaotic attractor. However at point BC2 the stable branch of 5T bifurcation group collides with the borderline and rapid chaotification is observed without the development of sequent period-doubling cascade.

The bifurcation map, shown in the Fig. 2, allows asserting that further increasing the value of S_c leads to the implementation of direct P2-P6, P2-P8, P2-P10 etc. transitions as well as the development of increasingly wider periodic windows, excluding the possibility of existence of practically useful robust chaotic modes of operation.

4. Conclusions

The results of complete bifurcation analysis allow revealing some interesting changes in chaotification scenario of the compensated boost switching power converter. For the converters with small output capacitance and without compensating ramp (i.e. S_c=0) the classical smooth period doubling route to chaos could be observed. As the value of the compensating ramp signal is increased the non-smooth effects, emerging from the interaction of bifurcation branches of stable and unstable periodic regimes with the borderline (4), take place, determining the general appearance of bifurcation diagram and transition to chaotic mode of operation.

It should be noted that, taking into account the topology of complete bifurcation diagrams constructed within this research, the definition of bifurcation group in MCBG (see e.g. [7]) should be revised, as the P2 and P4 regimes in the Fig. 4, corresponding to the same 1T bifurcation group have no common bifurcation points and are not mutually connected with stable or unstable branches.

Acknowledgements

References
1. M. Qin and J. Xu. Multiduty ratio modulation technique forswitching DC–DC converters operating in discontinuous conduction mode. *IEEE Trans. Ind. Electron.*, vol. 57, no. 10, 3497–3507, 2010.
2. J.H.B. Deane and D.C. Hamill. Improvement of power supply EMC by chaos. *Electron. Lett.*, vol. 32, no. 12, 1045-1049, 1996.

3. S. Banerjee and G. C. Verghese (Ed.) . *Nonlinear Phenomena in Power Electronics* . *Attractors, Bifurcations, Chaos, and Nonlinear Control*, IEEE Press, 2001.
4. M. di Bernardo, C.J. Budd, A.R. Champneys, P. Kowalczyk. *Piecewise-Smooth Dynamical Systems: Theory and Application*, Springer –Verlag, Berlin, 2008.
5. M. di Bernadro , E. Fosas, G. Olivar, F. Vasca. Secondary bifurcations and high-periodic orbits in the voltage controlled buck converter. *International Journal of Bifurcation and Chaos*, vol.12, no.7, 2755-2771, 1997.
6. D.C. Hammil, J.H.B. Deane, D.J. Jefferies. Modeling of chaotic dc/dc converters by iterative nonlinear mappings. *IEEE Transactions on Circuits and Systems Part I,* vol.35, no.8, 25-36, 1992.
7. M. Zakrzhevsky. New Concepts of Nonlinear Dynamics: Complete Bifurcation Groups, Protuberances, Unstable Periodic Infinitiums and Rare Attractors. *Journal of Vibroengineering*, vol.10, iss.4, 421-441, 2008.
8. D. Pikulins. Subharmonic oscillations and chaos in dc-dc switching converters. *Electronics and Electrical Engineering*, *Kaunas: Technologija*, 4: 33-36, 2013.
9. D. Pikulins. Effects of Non-Smooth Phenomena on the Dynamics of DC-DC Converters. S*cientific Journal of RTU: 4 series*, 29: 119-122, 2011.

Robustness of Chimera states in Nonlocally Coupled Logistic Maps

Pranneetha B[1] and Nita Parekh[2]

[1] Centre for Computational Natural Science and Bio-informatics, IIIT Hyderabad.
(E-mail: pranneetha.bellamkonda@students.iiit.ac.in)

[2] Centre for Computational Natural Science and Bio-informatics, IIIT Hyderabad.
(E-mail: nita@iiit.ac.in)

Abstract: In the last decade there has been considerable interest in a novel dynamical phenomenon of chimera states observed in an array of non-locally coupled oscillators where regions of coherence and incoherence coexist across the network. In this study we show how chimera states emerge in coupled logistic maps for certain specified initial conditions when the range and strength of coupling is varied. Here we show that these states are very robust and persist even in the presence of noise in the network parameters. On applying localized external perturbation to the incoherent regions, it is possible to obtain a completely coherent/incoherent dynamics in the whole network depending on the strength and sign of perturbation. This has important applications in the control of undesirable local dynamics, such as seizures in neural systems, or fibrillations in cardiac tissues.

Keywords: Chimera states, coupled logistic maps, control, pinning.

Introduction

The coexistence of coherent and incoherent dynamics in an array of non-locally coupled, identical Ginzburg Landau oscillators was first observed by Kuramoto and Battogtokh [1]. Such a state was named "chimera" meaning, something composed of incongruous parts. Chimera states are defined as spatiotemporal patterns of synchrony and disorder in homogeneous, non-locally coupled excitable systems. Recently, this phenomenon has been experimentally demonstrated in a system of mechanical oscillators by Aaron *et al* [2]. What makes the chimera behavior interesting is the coexistence of distinct spatial regions of synchronized behavior and irregular incoherent behavior, in networks of identical and symmetrically coupled units. Such a phenomenon is also observed in nature in neuronal systems of birds and dolphins which sleep with half of their brain (synchronous state) while the other half remains awake (asynchronous state) [3].

Network topologies such as global (i.e. all-to-all) coupling and local (i.e. nearest-neighbor) coupling have been extensively studied. However, networks with nonlocal coupling has been less studied in spite of applications in wide areas, *viz.*, chemical oscillators [4], excitable systems e.g., neural tissue [5], Josephson junctions [6], etc. There is now renewed interest in nonlocal networks with the recent discovery of chimera states [7]. In various numerical studies it has been shown that non-local coupling is a necessary condition for the occurrence of chimera states [8]; with local or global coupling, identical oscillators either synchronize or oscillate incoherently, but never do both simultaneously. In addition, the emergence of chimera states is extremely sensitive to the initial conditions and is observed only for carefully chosen initial conditions [9]. Numerous studies suggest that chimera states can exist in complex systems with nonlocal interactions. In this study we analyze the chimera states in nonlocally coupled logistic maps. Since it is unlikely that in any physical system, all the units are identical, the effect of heterogeneity on their collective behavior is of interest. With this objective we analyze the emergence and stability of chimera states in the presence of noise. In particular, we introduce noise in the initial conditions and in the system parameters, *viz.*, the bifurcation parameter and the coupling strength. In the event of undesirable dynamical behavior in localized regions, *viz.*, cardiac arrhythmia, epileptogenic neural activity, desynchronization in coupled chemical reactors, etc. With this objective we analyze the effect of external perturbation or pinning given selectively to regions of incoherence on the spatiotemporal dynamics of the whole system.

2 The Model and Simulations

Model:

In this study we analyze the occurrence of chimera states in non-locally coupled logistic maps on one-dimensional lattice (with periodic boundary conditions). We consider identical logistic maps at every node of the lattice which are coupled to P neighbors on either side on the spatial lattice. The spatio-temporal dynamical system considered here is given by the equation

$$x_j^{t+1} = (1 - \varepsilon) f(x_j^t) + \frac{\varepsilon}{2P} \sum_{j=i-P}^{i+P} f(x_j^t) \qquad (1)$$

where $i = 1, 2, \ldots, N$, t denotes the time step, ε the coupling strength and each node is coupled to P number of nodes on either side, i.e., a total of $2P$ connections. The local function considered here is a logistic map given by $f(x) = ax(1 - x)$, a being the bifurcation parameter. The radius of coupling $r_c = P/N$ is a constant for all the nodes in the lattice. Since $P = 1$ corresponds to local (nearest-neighbor) coupling and $P = N/2$ corresponds to global coupling (all nodes connected to all other nodes), r_c lies between $1/N$ and $1/2$. To

mathematically quantify how spatially coherent or incoherent certain region in the lattice is, the parameter R_i which gives the ***degree of coherence*** in a local region surrounding the node i is defined as

$$R_i = \lim_{N \to \infty} \frac{1}{2\delta} \left| \sum_{|j-i| \leq \delta} e^{i\psi_j} \right| \qquad (2)$$

where $i = 1, 2, ..., N$, $\psi_j = sin^{-1}(2x_j - max_j x_j - min_j x_j)/(max_j x_j - min_j x_j)$, δ denotes the neighborhood of a node on either side for which the extent of coherence is measured, $max_j x_j$ and $min_j x_j$ denote the maximum and minimum values of x_k respectively, where k is a node in the neighborhood of node j. R_i measures the degree of coherence in an interval defined by δ, in that as $N \to \infty$ and $\delta \to 0$, $R_i \to 1$ in the coherent interval and $0 < R_i < 1$ in the incoherent interval. In Figure 1(a) is shown the spatial dynamics of x at a given time t, after eliminating the transients. In Figure 1(b) is shown the spatial behavior of R for $\delta = 2$. It may be noted that the value of R in the coherent region is close to 1 in Figure 1(b) ($\delta = 2$). In the incoherent regions, the value of R is lower than in the coherent regions. Thus, analyzing the behavior of R_i helps in detecting the presence of chimera states in the lattice.
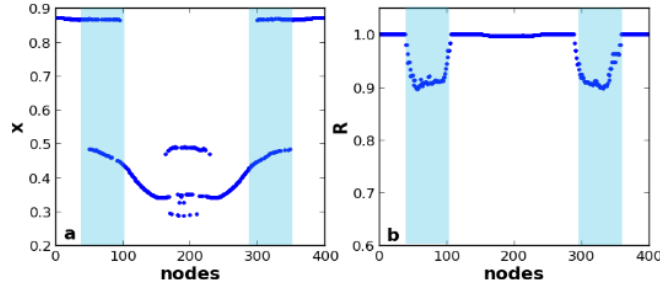

Fig. 1: a) Spatial dynamics of x for $\delta = 2$, b) spatial dynamics of R for $\delta = 2$. The system size $N = 400$, and the system parameters are $a = 3.8$, $r_c = 0.32$, $\varepsilon = 0.24$. Regions shaded in blue are the regions of incoherence.

Initial Conditions:

In numerous studies it has been shown that the emergence of chimera states is extremely dependent on the initial conditions. Here we consider three different initial distributions of x to induce chimera states in the 1d spatially coupled lattice.

TYPE I: In this case, the distribution of x in the initial state is set to be the same in certain regions of the lattice, and randomly distributed between an interval in small intervals between them as defined below and depicted in Figure 2(a) [1]:

$$i \in [0, N/8) \text{ and } [7N/8, N), x_i(0) = 0.45$$
$$i \in [N/4, 3N/4), x_i(0) = 0.9$$

$i \in [N/8, N/4)$ and $[3N/4, 7N/8)$, $x_i(0) \in I$, $I = [0.4, 0.5]$ U $[0.85, 0.95]$

After eliminating the transients we observe the emergence of chimera states in the lattice: the coherent regions corresponding to those with initial condition 0.45 and 0.9, and the incoherent regions interspersed in between them as seen in Figure 2(d). The spatial behavior of R in Figure 2(g) further confirms the chimera state. It is important to start the system with some regions in distinctly different initial conditions to observe the chimera behavior.

TYPE II: A half compressed *tanh* function in the first half of the lattice and its mirror image in the second half as shown in Figure 2(b) is considered and is given by

$$i \in [0, N/2), \ x_i(0) = \frac{1}{2}\left(\tanh\left(\frac{3(i - N/4)}{N/4} \right) + 1 \right)$$

$$i \in [N/2, N), \ x_i(0) = \frac{1}{2}\left(\tanh\left(\frac{3(3N/4 - i)}{N/4} \right) + 1 \right)$$

The chimera behavior is observed in this case also as shown in Figure 2(e) and 2(h), very similar to that observed with type I initial conditions, except that the incoherent intervals are not so well defined.

TYPE III: In this case the initial distribution of x is considered to be a sine function over the lattice given by

$$i \in [0, N), \ init \ x_i = \sin(i\pi/N)$$

as shown in Figure 2(c). The spatial behavior of x in Figure 2(f) and R_i is Figure 2(i) exhibits emergence of chimera states. Unlike type I and type II conditions, in this case there is no sharp discontinuity in the x value along the lattice, and also has no interval that is completely coherent (region in which every node has a constant value). In the case of type II or type III initial conditions, the chimera states are observed only when the local dynamics is chaotic, while the type I initial conditions give rise to chimera states even when the local dynamics is periodic; in this case the regions of incoherence are spatially and temporally periodic while the coherent regions are spatially synchronous. Thus we observe that different types of initial conditions can give rise to chimera states, as long as the coupling is non-local.
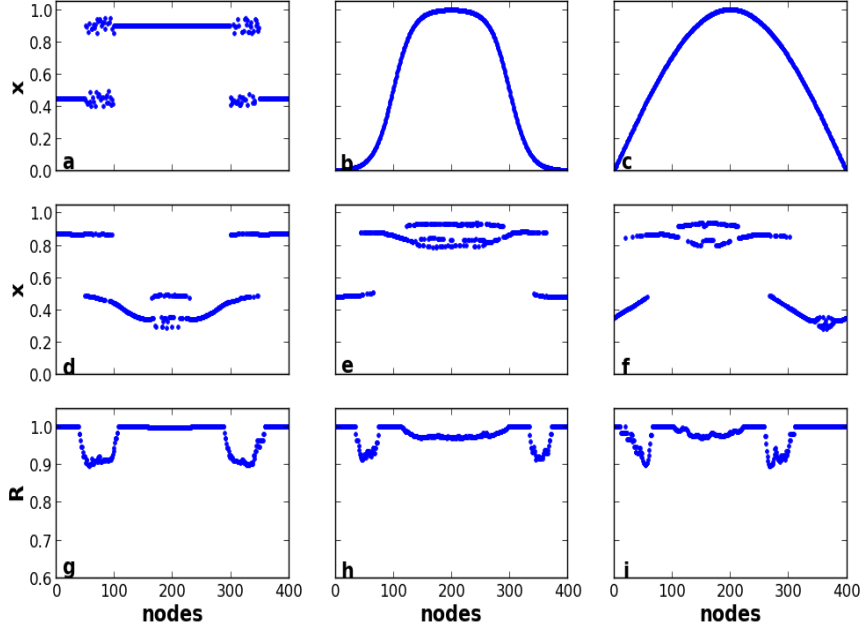
Fig. 2: The three types of initial conditions considered here, *viz.*, type I, II and III, are shown in (a) – (c) and in (d) – (f) the spatial dynamics of non-locally coupled logistic maps obtained after eliminating 50000 transients for the corresponding initial conditions is depicted. Figures (g) – (i) depicts the spatial dynamics of R corresponding the to the dynamics of x in (d) – (f) respectively. The parameters (r_c, ε) for the plots (d), (g) are (0.32, 0.24), (e), (h) are (0.24, 0.24) and (f), (i) are (0.24, 0.24).

Sensitivity to initial conditions:

In order to see the dependence on the initial conditions for the emergence of chimera states, in Figure 3 we show the spatio-temporal dynamics of the system after eliminating 50000 transients for the parameters chosen in the chaotic regime. In Figure 3(a) is shown the dynamical state attained on using type I initial conditions (defined above) and in Figure 3(b) dynamical state attained on using random initial, i.e. $x_i(0)$ is a random number in the range (0,1). It may be noted that in Figure 3(a) with type I initial conditions, the system exhibits regions of incoherence interspersed between regions of coherence, while no such dynamical behavior is observed with random initial conditions (Figure 3(b)), for same set of parameter values. The spatio-temporal dynamics of the lattice was analyzed for 50 different random initial configurations and chimera behaviour was not observed in any of these cases. Thus we may conclude that though the emergence of chimera behaviour is sensitive to initial conditions, it is observed for a various types of carefully chosen initial conditions.
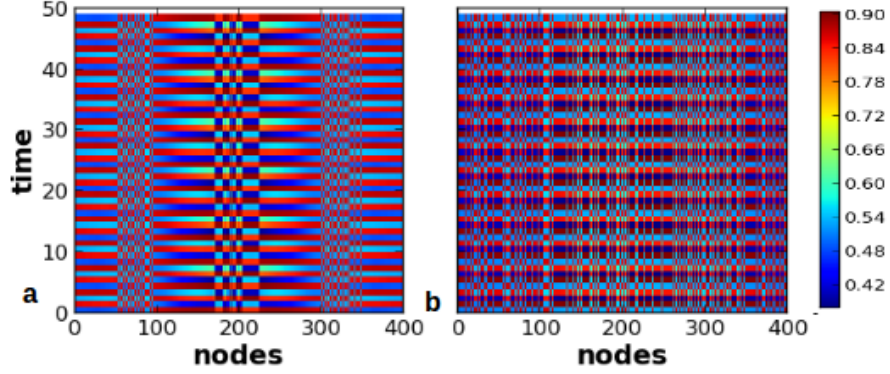
Fig. 3: Spatio-temporal dynamics of the non-locally coupled logistic maps with (a) type I initial conditions, (b) random initial conditions in the interval (0, 1) for $a = 3.8$, $r_c = 0.32$ and $\varepsilon = 0.24$.

3 Results and Discussions:

Analysis of r_c - ε parameter space:

The emergence of chimera states is observed to be dependent on two parameters, *viz.*, the range of coupling, r_c and the strength of coupling, ε. In Figure 4 is shown the r_c - ε parameter-space plot indicating various dynamics observed in one-dimensional non-locally coupled logistic maps for type I initial conditions. The chimera behavior is observed for a wide range of coupling shown by regions in blue when the coupling strength ε is low and K denotes the wave number of the spatial dynamics. It is observed that for a given coupling strength, chimera states with higher wave numbers occur at lower radius of coupling than those with lower wave numbers. Also, with increase in the range of coupling r_c, the chimera behavior is observed even for very lower coupling strengths, ε. The red and green regions correspond to temporally periodic dynamics with period $p = 4$ and 2 respectively. The yellow region corresponds to chimera dynamics with $p = 4$, while the purple region indicates chimera dynamics with $p = 2$.
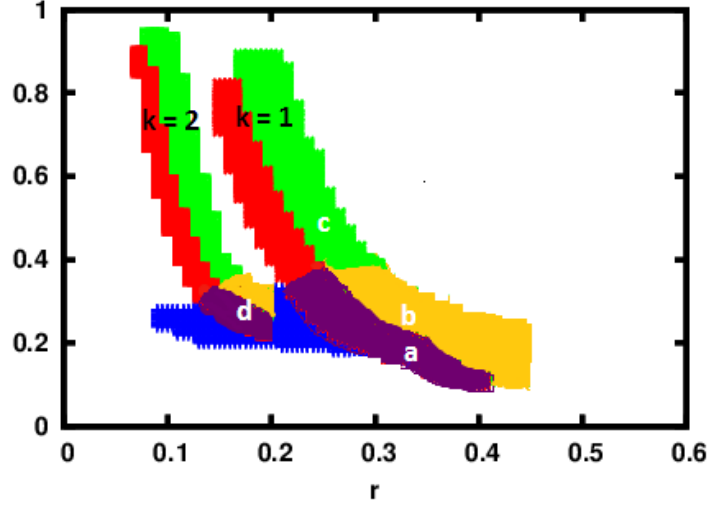
Fig. 4: r_c - ε parameter-space plot shown for non-locally coupled logistic maps with $N = 400$ with type I initial conditions. The values of a is 3.8. The chimera states emerge in regions shown in blue, purple and yellow, while red and green regions correspond to temporal periodic dynamics with period-4 and period-2 respectively. The yellow region indicates intersection of blue and green regions and purple region, the intersection of blue and red regions. K denotes the wave number of the spatial dynamics.

In Figure 5 the spatiotemporal dynamical behavior of the system at points marked 'a', 'b', 'c', and 'd' in Figure 4 is depicted in the third column. It may be noted from the spatio-temporal dynamics of x corresponding to point 'a' and 'b' that as the coupling strength ε increases from 0.2 to 0.24, the degree of coherence increases (for fixed $r_c = 0.32$). On further increasing the coupling strength ($\varepsilon > 0.3$), the regions of incoherence disappear and the lattice is seen to exhibit coherent dynamics (results not shown). The spatio-temporal dynamics at larger coupling strength, $\varepsilon = 0.42$ ($r_c = 0.24$) corresponding to 'c' is mainly coherent. The spatio-temporal dynamics corresponding to point 'd' exhibits higher wave number (K = 2) and period (p = 4).

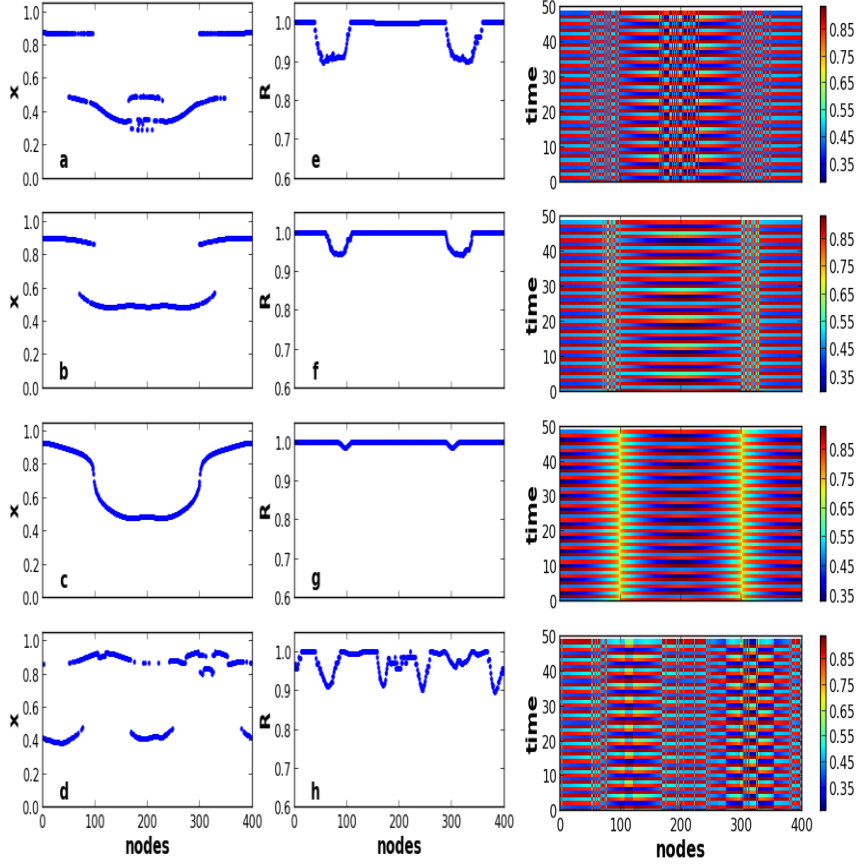Fig. 5: (a) - (d) depicts the spatial dynamics (x_i vs i) at points a, b, c and d respectively in the r_c - ε parameter-space plot (Figure 4). (e) – (h) spatial plots of R_i vs i corresponding to the plots (a) – (d). The parameter values (r_c, ε) for the points 'a', 'b', 'c', and 'd' in Figure 4 correspond to (0.32,0.2), (0.32, 0.24), (0.28,0.42) and (0.15, 0.24) respectively. The points 'a', 'b', and 'c' corresponds to wave number $K = 1$, while point 'd' to wave number $K = 2$. The spatiotemporal dynamics is shown in the third column. For the calculation of R, δ value was chosen to be 2.

Thus we observe that for fixed coupling strength ε, the incoherence in the spatial dynamics decreases with an increase in the radius of coupling. This is confirmed from the spatial behavior of degree of coherence, R_i, for different values of radius of coupling in Figure 6(a). Similarly, for weak coupling the dynamics is incoherent, but as the coupling strength is increased through a critical value (for fixed radius of coupling), coherence emerges and on further

increase in the coupling strength, complete synchronization is observed. This is quantified in terms of R_i in Figure 6(b).
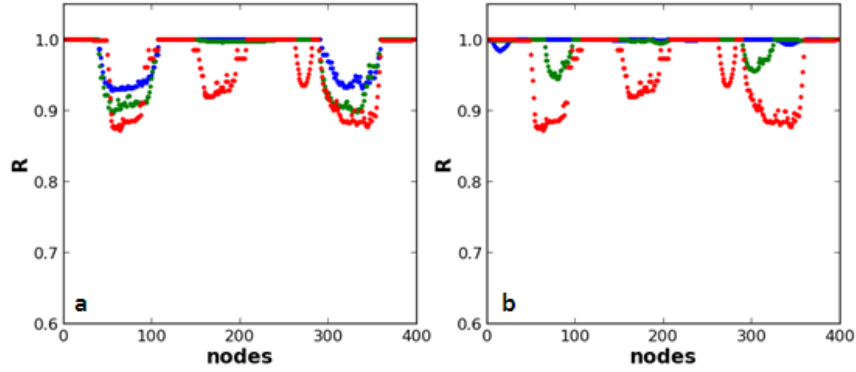

Fig. 6: (a) Spatial behavior of R is shown for various values of radius of coupling, r_c: 0.2 (red), 0.32 (green) and 0.4 (blue) for a constant coupling strength, $\varepsilon = 0.24$. There is a clear decrease in the spatial incoherence with increase in the value of r_c. (b) Spatial behavior of R is shown for various values of coupling strength, ε : 0.24 (red), 0.32 (green) and 0.36 (blue) for a constant , $r_c = 0.2$. We see a clear decrease in the degree of spatial incoherence with increase in the value of ε. The remaining parameters for figures 6(a),(b) are $a = 3.8$, $N = 400$, $\delta = 2$.

Robustness of chimera states to perturbations :

In real practical situations, it is unlikely to have the same system parameters over the entire spatial domain, e.g., the junctional coupling strengths, ε may vary between cells in a neural tissue, or the growth parameter a may not be same in all subpopulation patches, etc. To mimic such a scenario, we introduce small random variations in the system parameters a and ε, i.e., $a \pm \delta a_i$ and $\varepsilon + \delta \varepsilon_i$. Since the occurrence of chimera states is sensitive to the initial conditions, we also introduce noise in the initial conditions, i.e., $x_i(0) \pm \delta x_i(0)$ ($x_i(0)$ refers to type I initial conditions), and analyze the emergence and stability of the chimera states in such a heterogeneous coupled logistic maps. In Figure 7(a)-(d) is shown the spatial dynamics of x and in the adjacent plots (2nd panel) the spatio-temporal dynamics for varying coupling strengths. It is observed that at lower coupling strengths, the lattice exhibits incoherent dynamics in the presence of noise. As the coupling strength is increased, incoherence in the dynamics is reduced and emergence of chimera states is clearly observed for intermediate coupling strengths (0.24 < 0.35). For $\varepsilon > 0.35$, the lattice exhibits spatially coherent dynamics.
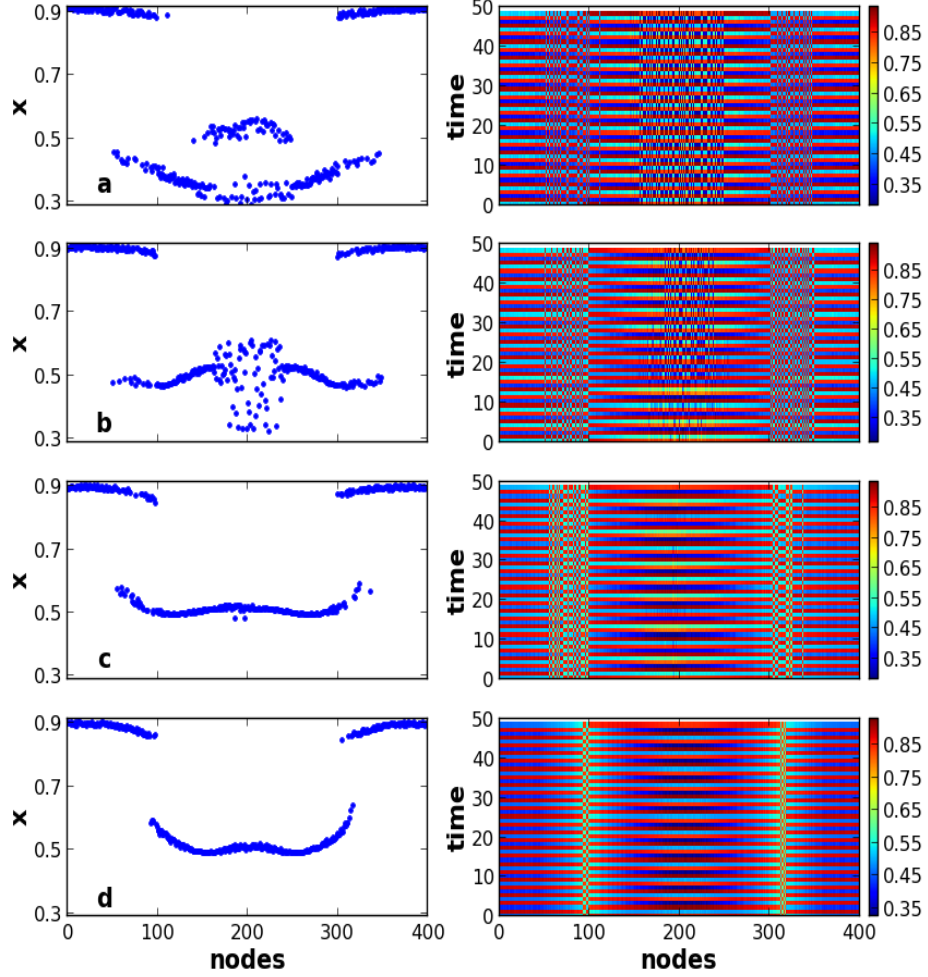
Fig. 7: In (a) – (d) is shown the spatial dynamics of *x* and their corresponding spatio-temporal plots (in the 2nd column) for different coupling strengths, $\varepsilon = 0.2, 0.24, 0.3$ and 0.35 respectively with a variation of ± 0.005. The parameters values of the lattice are $a = 3.8 \pm 0.04$, and the random variations to the type I initial conditions as ± 0.05.

Effect of External Perturbation on the Chimera States:

In various physical and biological systems such as power grids or excitable tissues (e.g., cardiac or neuronal tissues), the synchronous movement of all their parts is extremely crucial for their proper functioning [10]. Localized regions of incoherence in such systems may cause hindrance to their performance and in extreme situations may even completely destabilize the system [11]. In such situations, there is clearly a need to address local disturbances/incoherent

dynamics and bring the system back to its original synchronous dynamical state. Here we attempt to analyze the effect of applying localized external perturbation or "pinning" to the incoherent regions and see if the system is driven to spatially synchronous state or the whole lattice exhibits incoherent dynamics. The objective is to manipulate the dynamics in the event of the system exhibiting undesired local dynamics. For example, extended periods of synchronization in the brain, results in epileptic seizures and there exists need for external intervention. In diffusively coupled logistic maps, it has been shown by Parekh *et al* [12] that negative pinning suppresses chaos while positive pinning induces/enhances chaos. In Figure 8(a), we observe that on applying negative pinning to the incoherent regions, the degree of incoherence is reduced and can be completely suppressed, while applying positive pinning as shown in Figure 8(b), the degree of incoherence is enhanced. However, it may be noted that the coherent dynamics attained by selectively pinning the regions of incoherence exists only as long as the pinning is being given. In Figure 9 is shown the effect of removing the external pinning after having applied for a certain period of time. Initially the system is considered to be exhibiting chimera behavior when no pinning is applied to (blue). The region of incoherence is decreased both in the spatial spread and extent on applying negative pinning selectively to the nodes in the incoherent region (red). On switching off the external pinning and eliminating transients, we observe that the system goes back to the original dynamical state and exhibits spatial incoherence regions which are much narrower than the initial case, i.e., on switching off the external perturbation, the extent of spread of the incoherent dynamics is reduced, but not completely eliminated.
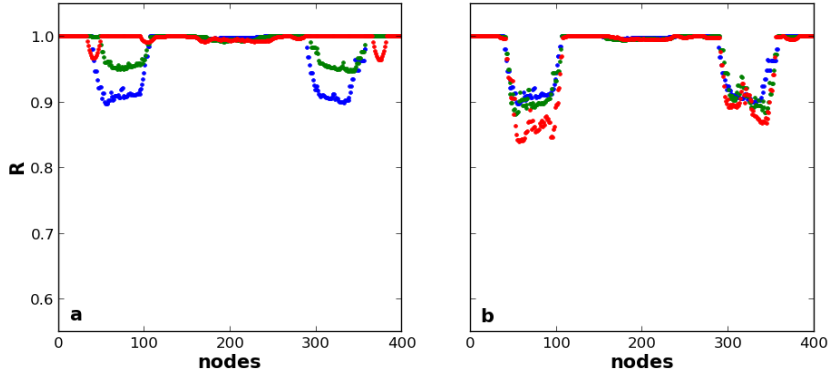

Fig. 8: (a) Spatial behavior of R for the parameters $N = 400$, $r_c = 0.32$, $\varepsilon = 0.24$, $\delta = 2$, shown on selectively pinning the incoherent regions with varying strengths of (a) negative pinning: -0.05 (green) and -0.15 (red); (b) positive pinning: 0.02 (green), 0.05 (red). The plots in blue correspond to "no pinning"

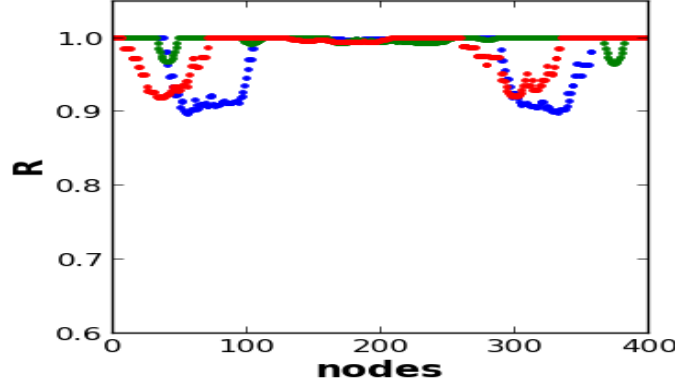in both (a) and (b). It is clear that negative pinning suppresses while positive pinning enhances incoherence.

Fig. 9: Spatial behavior of R: i) no pinning (blue), ii) selective pinning of - 0.13 (green) after eliminating 50000 transients and iii) eliminating 50000 transients after removing the selective pinning (red). Here, $a = 3.8$, $N = 100$, $r_c = 0.32$, $\varepsilon = 0.18$, $\delta = 2$.

Conclusions

In this study we carried out a systematic analysis for the emergence and stability of chimera behavior in non-locally coupled logistic maps. We discuss the emergence and disappearance of chimera states as a function of the radius and strength of coupling. The chimera states are observed to be robust to small random variations in the initial conditions and system parameters for reasonable strength and radius of coupling. We also showed that is possible to suppress/induce incoherence in spatially localized regions as this maybe desirable in certain situations such as epileptic seizures, or cardiac fibrillation. However, the persistence of pinning is required for achieving the desired behavior. This has important applications in many complex physical and biological systems.

References

1. Kuramoto and Battoghtokh, *Complex Systems 5, 380* (2002).
2. Aaron M. Hagerstrom, Thomas E. Murphy, Rajarshi Roy, Phillip Hovel, Iryna Omelchenko, Eckehard Scholl, *Nature Physics Vol. 8 pg no. 658-661* (2012).
3. C. G. Mathews, J. A. Lesku, S. L. Lima, C. J. Amlaner, *Ethology 112, 286* (2006).
4. A. S. Mikhailov and K. Showalter, Phys. Rep. 425, 79 (2006).

5. R. Vicente, L. L. Gollo, C. R. Mirasso, I. Fischer, and P. Gordon, Proc. Natl. Acad. Sci. 105, 17157 (2008)

6. K. Wiesenfeld, P. Colet, and S. H. Strogatz, Phys. Rev. Lett. 76, 404 (1996).

7. O. E. Omel'chenko, M. Wolfrum, and Y. L. Maistrenko, Phys. Rev. E 81, 065201 (2010).

8. Daniel M Abrams, Steven H Strogatz, *Chaos, Vol. 16,* (2006).

9. Iryna Omelchenko, Yuri Maitsrenko, Philipp Hovel, Eckehard Scholl, *PRL Vol. 106,234102* (2011).

10. Martin Rohden, Andreas Sorge, Marc Timme, Dirk Witthaut, Phys. Rev. Lett. *Vol. 109,064101* (2012).

11. Erik A Martens, Shashi Thutupalli, Antoinne Fourriere, Oskar Hallatschek, *National Academy of Sciences, Proceedings, Vol. 110, issue no. 26* (2013).

12. Nita Parekh, S. Parthasarathy, Somdatta Sinha, Phys. Rev. Lett. *Vol. 81. pg no. 1402* (1998).